

¹
² Susceptible host dynamics explain pathogen resilience to
³ perturbations

⁴
⁵ Sang Woo Park, . . . , Sarah Cobey

⁶ Abstract

⁷ Major priority for epidemiological research in the time of anthropogenic change is
⁸ understanding how infectious disease dynamics respond to perturbations. Interven-
⁹ tions to slow the spread of SARS-CoV-2 significantly disrupted the transmission
¹⁰ of other human pathogens. As interventions lifted, whether and when respiratory
¹¹ pathogens would eventually return to their pre-pandemic dynamics remains to be
¹² answered. To address this gap, we develop a framework for estimating pathogen re-
¹³ silience based on how fast epidemic patterns return to their pre-pandemic, endemic
¹⁴ dynamics. Our analysis suggests that some pathogens may have settled to endemic
¹⁵ cycles that are different from their pre-pandemic patterns. Finally, we show that
¹⁶ the replenishment rate of the susceptible pool is a key determinant of pathogen re-
¹⁷ silience. Our framework offers a novel perspective to characterizing the dynamics of
¹⁸ endemic pathogens and their responses to SARS-CoV-2 interventions. [SWP: Need
¹⁹ to emphasize broader implications.]

20 [SWP: *There was substantial uncertainty about the dynamics of non-COVID
21 pathogens in the wake of 2020, and we saw different patterns of return in different
22 countries, and we don't have a good theory to understand if we should see persistent
23 differences. We now see signals of some persistent differences, but too soon to say
24 for many.*]

25 Non-pharmaceutical interventions (NPIs) to slow the spread of SARS-CoV-2 dis-
26 rupted the transmission of other human pathogens, providing large-scale natural
27 experiments for understanding how various host-pathogen systems respond to pertur-
28 bations [1, 2, 3, 4]. As interventions lifted, large heterogeneities in outbreak dynam-
29 ics were observed across different pathogens in different countries (Figure 1). These
30 heterogeneities raised questions about what factors determine these re-emergence
31 patterns and whether we will see persistent changes in pathogen dynamics following
32 the pandemic [5, 6, 7]. However, a limited understanding of pre-pandemic dynam-
33 ics of common respiratory pathogens have so far limited our ability to answer these
34 questions and further tease apart how different factors contribute to heterogeneities
35 in their re-emergence patterns.

36 More than five years have passed since the emergence of SARS-CoV-2, and we
37 now have potential evidence for fundamental changes in pathogen dynamics following
38 the pandemic, which likely reflect permanent changes in either human behavior or
39 population-level immunity [5, 6]. For example, compared to pre-pandemic, seasonal
40 patterns, human metapneumovirus and bocavirus in Korea are circulating at lower
41 levels, whereas RSV in Korea seem to exhibit different seasonality (Figure 1). These
42 observations pose two fundamental questions for current and future infectious disease
43 dynamics: (1) can we learn about underlying pathogen characteristics, such as their
44 transmissibility or duration of immunity, from re-emergence patterns? and (2) can
45 we predict whether and when other respiratory pathogens will eventually return to
46 their pre-pandemic dynamics?

47 Understanding how ecological systems respond to perturbations is a fundamental
48 challenge in predicting population persistence and extinction [8, 9, 10]. These re-
49 sponds can be characterized in terms of resilience, which often measures how fast a
50 system returns to its stable, reference state following a perturbation [11, 12, 13, 14].
51 Theoretical and empirical efforts to quantify resilience of ecological systems have pro-
52 vided key insights for understanding the dynamics of complex systems and linking
53 these findings to actionable strategies for species conservation [15]. However, de-
54 spite rich literature on ecological resilience, there have been limited applications to
55 measuring the resilience of host-pathogen systems, especially for human pathogens.

56 To address this question, we propose a framework for characterizing the resilience
57 of a host-pathogen system based on how fast the system recovers from perturbation.
58 We begin by laying out a few representative scenarios that capture the potential im-
59 pact of COVID-19 interventions on endemic pathogen dynamics and illustrating how
60 resilience can be measured by comparing the pre- and post-pandemic dynamics of
61 susceptible and infected hosts. In practice, information on susceptible hosts are often
62 unavailable, and traditional methods for reconstructing the dynamics of susceptible

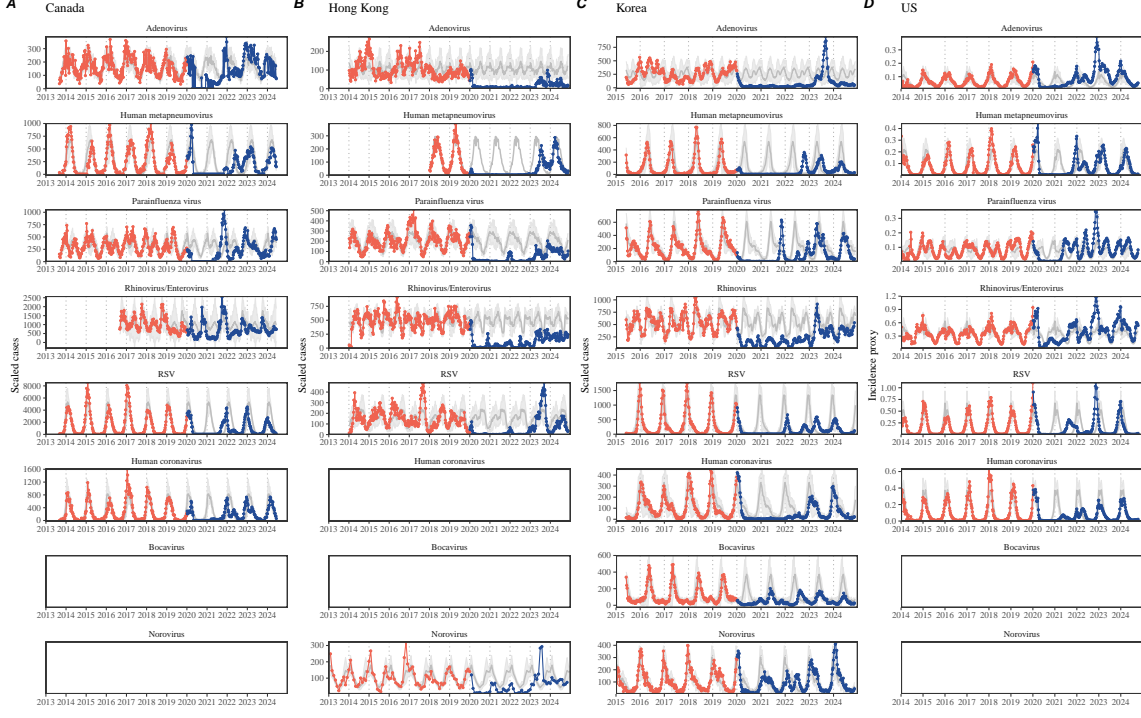


Figure 1: Observed heterogeneity in responses to COVID-19 pandemic across respiratory pathogens and norovirus in (A) Canada, (B) Hong Kong, (C) Korea, and (D) US. Red points and lines represent data before 2020. Blue points and lines represent data since 2020. Gray lines and shaded regions represent the mean seasonal patterns and corresponding 95% confidence intervals based on the observed outbreak patterns before 2020.

hosts require long-term endemic time series [16, 17], which cannot be applied due to disruptions in epidemic patterns caused by COVID-19 interventions. Instead, we utilize Takens’ embedding theorem to reconstruct empirical attractors from data and further measure the distance from this empirical attractor [18]. This reconstruction allows us to characterize the rate at which this distance decreases over time, which correspond to pathogen resilience. We apply this framework to analyzing pathogen surveillance data for a wide array of respiratory and non-respiratory pathogens from Canada, Hong Kong, Korea, and US. Finally, we show that susceptible host dynamics are a key determinants of pathogen resilience. Our study offers unique insights into understanding pathogen re-emergence patterns following COVID-19 interventions.

Conceptual introduction to pathogen resilience

In classical ecological literature, resilience of an ecological system is measured by the rate at which the system returns to its reference state following a perturbation [11, 12, 13, 14]. This rate corresponds to the largest real part of the eigenvalues of

77 the linearized system near equilibrium—here, we refer to this value as the *intrinsic*
78 resilience of the system, which represents the expected rate of return from perturbed
79 states. However, respiratory pathogens often exhibit seasonal variation in transmission,
80 meaning that the intrinsic resilience of a host-pathogen system varies across
81 season. Nonetheless, we can still measure the *empirical* resilience of a host-pathogen
82 system by looking at how fast the system returns to the pre-pandemic, endemic
83 dynamics after interventions are lifted.

84 As an example, consider an intervention that reduce transmission by 50% for 6
85 months starting in 2020, which causes epidemic patterns to deviate from its original
86 stable annual cycle for a short period of time and eventually come back (Figure 2A).
87 To measure the empirical resilience of this system, we first need to be able to measure
88 the distance from its pre-pandemic attractor. There are many different ways we can
89 measure the distance from attractor, but for illustrative purposes, we choose one of
90 the most parsimonious approach: that is, we look at how the susceptible (S) and
91 infected (I) populations change over time and measure the distance on the SI phase
92 plane (Figure 2B). In this simple case, the locally estimated scatterplot smoothing
93 (LOESS) fit indicates that the distance from attractor decreases linearly on average
94 (Figure 2C). Furthermore, the overall rate of return matches the intrinsic resilience
95 of the seasonally unforced system (Figure 2C).

96 Alternatively, NPIs can permanently change our behavior and have persisting
97 impact on the pathogen dynamics; as an example, we consider a scenario in which a
98 10% reduction in transmission persists even after the NPIs are lifted (Figure 2D–F).
99 In such cases, we cannot know whether the pathogen will return to its original cycle
100 or a different cycle until many years have passed after the NPIs are lifted, meaning
101 that we cannot measure the distance against the new attractor that the system will
102 eventually approach. Nonetheless, we can still measure the distance against the orig-
103 inal, pre-pandemic attractor and ask how the distance changes over time (Figure 2E).
104 The LOESS fit suggests that the distance from the attractor will initially decrease
105 exponentially on average (equivalently, linearly on a log scale) and eventually plateau
106 (Figure 2F). Here, a permanent 10% reduction in transmission rate slows down the
107 system, which causes the distance from the attractor to decrease at a slower rate
108 (Figure 2F) than it would have otherwise in the absence of permanent transmission
109 reduction (Figure 2C). This example shows that resilience is not necessarily an in-
110 trinsic property of a specific pathogen. Instead, pathogen resilience is a property of
111 a specific attractor that a host-pathogen system approaches, which depends on both
112 pathogen and host characteristics.

113 Finally, transient phenomena can also complicate the picture (Figure 2G–I). For
114 example, a stage-structured model for RSV initially exhibits a stable annual cycle,
115 but perturbations from NPIs cause the epidemic to exhibit biennial cycles (Figure
116 2G). Despite this biennial cycle, we see that the system eventually approaches the
117 original pre-pandemic attractor (Figure 2H), suggesting that this biennial cycle is a
118 transient phenomenon. The LOESS fit indicates that the distance from the attractor
119 will initially decrease exponentially at a rate that is consistent with the intrinsic

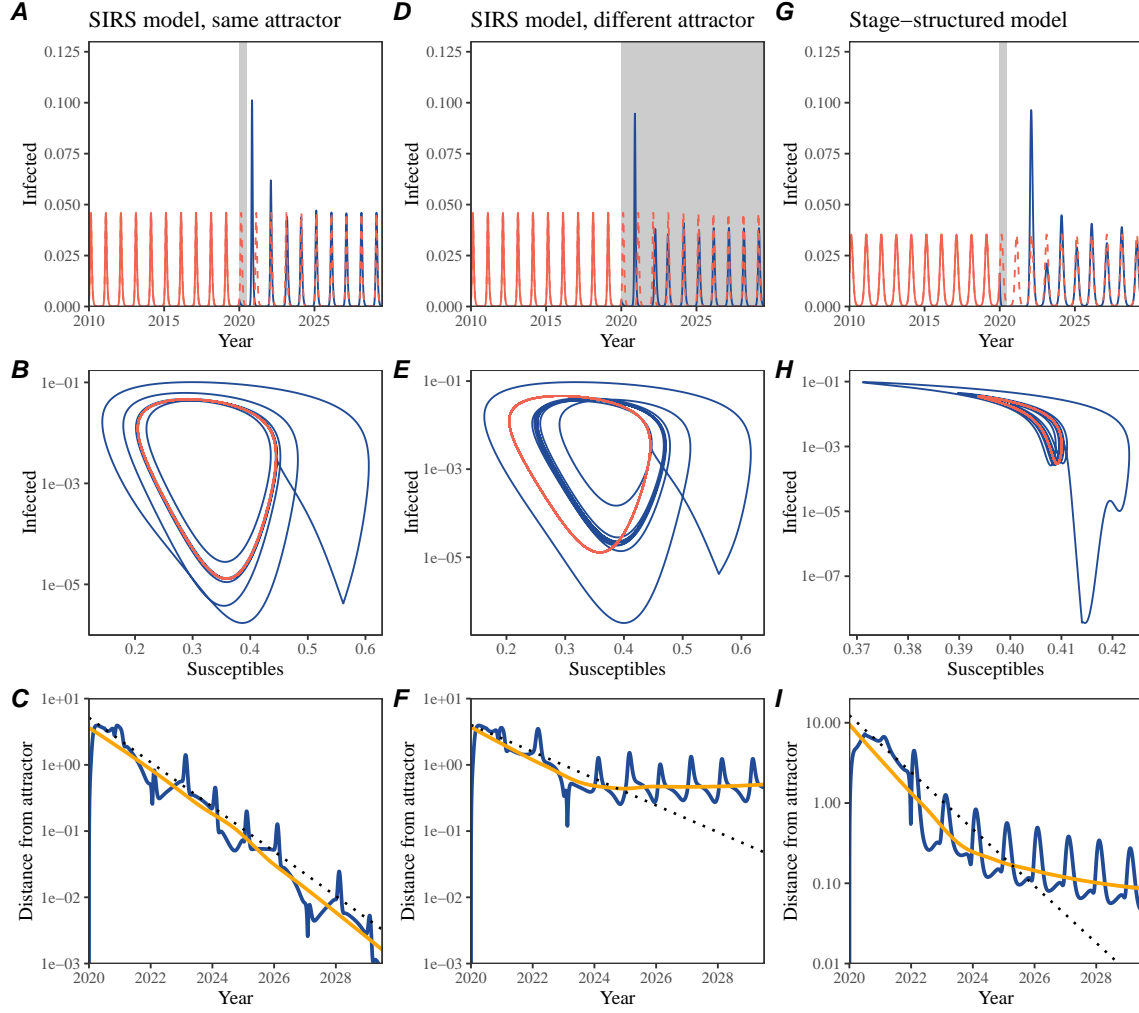


Figure 2: Conceptual framework for measuring pathogen resilience following NPIs across different scenarios. (A, D, G) Simulated epidemic trajectories across various models. Red and blue solid lines represent epidemic dynamics before and after interventions are introduced, respectively. Red dashed lines represent counterfactual epidemic dynamics in the absence of interventions. Gray regions indicate the duration of interventions. (B, E, H) Phase plane representation of the corresponding model. Red and blue solid lines represent epidemic trajectories on an SI phase plane before and after interventions are introduced, respectively. (C, F, I) Changes in logged distance from attractor over time. Blue lines represent the logged distance from attractor. Orange lines represent the locally estimated scatterplot smoothing (LOESS) fits to the logged distance from attractor. Dotted lines are superimposed as a comparison to have the same slope as the intrinsic resilience of the seasonally unforced system.

resilience of the seasonally unforced system, but the rate of decrease slows down

as the epidemic exhibits a biennial cycle (Figure 2I). In classical ecological theory, this behavior is also referred to as a ghost attractor, which causes long transient dynamics and slow transitions [19]. As we show in Supplementary Figure S1, strong seasonal forcing in transmission can also lead to transient phenomena for a simple SIRS model, causing a slowing down of the system.

In Supplementary Materials, we also explore measuring the resilience of a two-strain host-pathogen system: when the dynamics two strains (or two pathogens) are coupled through cross immunity, we would expect the entire system to be characterized by a single resilience value (rather than having two separate resilience for each strain). Simulations from a simple two-strain system illustrate that separate analyses of individual strain dynamics (e.g., RSV A vs B) and a joint analysis of total infections (e.g., total RSV infections) yield identical resilience estimates, confirming our expectation (Supplementary Figure S2, 3). Analogous to a single system, strong seasonal forcing in transmission can cause the system to slow down through transient phenomena (Supplementary Figure S4).

These observations indicate three possibilities. First, we can directly estimate the empirical resilience of a host-pathogen system by looking at how fast the system approaches a pre-pandemic attractor, provided that we can measure the distance from attractor. The empirical approach to estimating pathogen resilience is particularly convenient because it does not require us to know the true underlying model. As we show in Supplementary Figure S5, estimating the intrinsic resilience from fitting standard compartmental models can lead to biased estimates, especially under model misspecification. Second, resilience estimates allow us to make phenomenological predictions about the dynamics of a host-pathogen system following a perturbation: assuming that the distance from the attractor will decrease exponentially over time, we can obtain a ballpark estimate for when the system will reach an attractor. Finally, deviation from an exponential decrease in the distance from attractor can provide information about whether the system has reached an alternative attractor, or a ghost attractor, that is different from the original, pre-pandemic attractor. These alternative attractors may reflect continued perturbations from permanent changes in transmission patterns as well as changes in immune landscapes.

Inferring pathogen resilience from real data

Based on these observations, we now set out to infer pathogen resilience from real data. Here, we briefly lay out our approach to estimating pathogen resilience from real data (Figure 3). We then test this approach against simulations and apply it to real data.

So far, we focused on simple examples that assume a constant transmission reduction. However, in practice, the impact of NPIs on pathogen transmission is likely more complex (Figure 3A), reflecting introduction and relaxation of various intervention strategies. These complexities can lead to longer delays between the

introduction of NPIs and pathogen re-emergence as well as temporal variation in outbreak sizes (Figure 3B): in this example, continued transmission reduction from NPIs limits the size of the first outbreak in 2021 following the emergence, allowing for a larger outbreak in 2022 when NPIs are further relaxed.

Previously, we relied on the dynamics of susceptible and infected hosts to compute the distance from attractor (Figure 2), but information on susceptible hosts are often not available in practice. In addition, uncertainties in case counts due to observation error as well as the possibility of complex, multiannual attractor adds challenges to measuring the distance from attractor. To address these challenges, we first reconstruct an empirical attractor by utilizing Takens' theorem, which states that an attractor of a nonlinear multidimensional system can be mapped onto a delayed embedding [18]. Here, we use delayed copies of logged values of pre-pandemic cases $C(t)$ (Figure 3C) to reconstruct the attractor:

$$\langle \log(C(t) + 1), \log(C(t - \tau) + 1), \dots, \log(C(t - (M-1)\tau) + 1) \rangle, \quad (1)$$

where the delay τ and embedding dimension M are determined based on autocorrelations and false nearest neighbors, respectively [20, 21]. We then apply the same delay and embedding dimensions to the entire time series to determine the position on a multi-dimensional state space (Figure 3D), which allows us to measure the nearest neighbor distance between the current state of the system and the empirical attractor (Figure 3E). In principle, we can quantify how fast this distance decreases by fitting a linear regression on a log scale, where the slope of the linear regression corresponds to pathogen resilience. As we show in Supplementary Figure S6, overall temporal variations in the distance from attractor, especially the observed rate of decrease, appear robust to choices about embedding delays and dimensions; we note that using longer delays and higher dimensions tend to smooth out temporal variations in the distance from attractor.

186 Complex changes in the distance from attractor suggest that estimating pathogen
187 resilience from linear regression will likely be sensitive to our choice of fitting windows
188 for the regression. In Supplementary Materials, we explore an automated window
189 selection criteria for linear regression and test it against randomized, stochastic sim-
190 ulations across a wide range of realistic NPI shapes. We find that resilience estimates
191 based on the automated window selection criteria are moderately correlated (0.48)
192 with the intrinsic resilience of the post-NPI attractor (Supplementary Figure S7). In
193 contrast, a naive approach that uses the entire time series, starting from the peak
194 distance, only gives a correlation of 0.09 and consistently underestimates the intrinsic
195 resilience (Supplementary Figure S7).

Now, we apply this approach to pathogen surveillance data presented in Figure 1. For each time series, we apply Takens' theorem independently to reconstruct the empirical attractor and obtain the corresponding time series of distance from attractors (Supplementary Figure S8 for the distance time series and linear regression fits). Then, we use the automated window selection criteria to fit a linear regression and estimate the empirical resilience for each pathogen in each country. For most res-

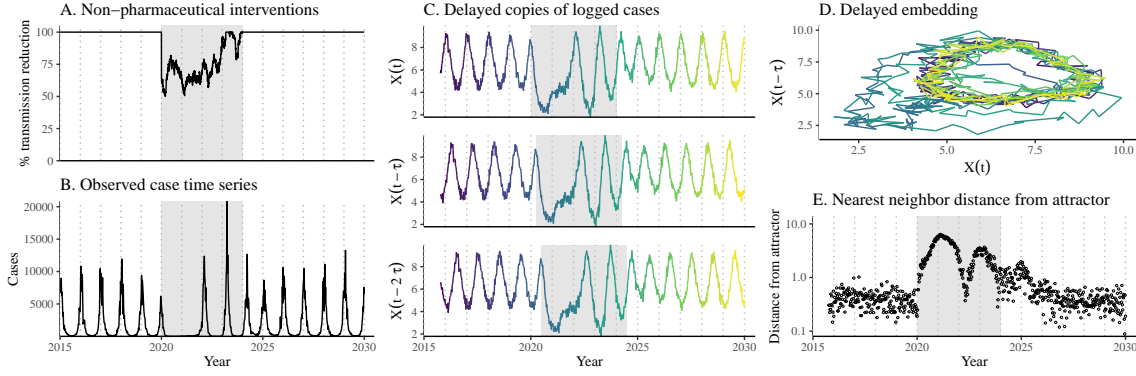


Figure 3: A schematic diagram explaining how pathogen resilience can be inferred from real data. (A) A realistic example of a synthetic NPI, represented by a relative reduction in transmission. (B) The impact of the synthetic NPI on epidemic dynamics simulated using a stochastic SIRS model. (C) Generating delayed copies of the logged time series allows us to obtain an embedding. (D) Two dimensional representation of an embedding. (E) Delayed embedding allows us to calculate the nearest neighbor distance from the empirical attractor, which is determined based on the pre-pandemic time series. This distance time series can be used to infer pathogen resilience by fitting a linear regression after choosing an appropriate window for regression.

piratory pathogens, resilience estimates fall between 0.4/year and 1.8/year (Figure 4A), with the exception of Rhinovirus in the US (0.066/year; 95% CI: 0.018/year–0.113/year) and Bocavirus in Korea (0.087/year; 95% CI: 0.023/year–0.151/year). Excluding these exceptions, the mean resilience of common respiratory pathogens is 0.974/year (95% CI: 0.784/year–1.16/year). As a reference, this is \approx 7 times higher than the intrinsic resilience of pre-vaccination measles dynamics (\approx 0.13/year). Finally, resilience estimates for norovirus appears to be comparable to the intrinsic resilience of measles: 0.119/year (95%CI: 0.004/year–0.233/year) for Korea and 0.385/year (95% CI: 0.167/year–0.603/year). A simple ANOVA shows that there are significant differences in resilience estimates across countries ($p < 0.036$) and pathogens ($p < 0.030$).

Using resilience estimates, we now predict when each pathogen will return to their original pre-pandemic cycles. Specifically, we extend our linear regression fits to distance-from-attractor time series and ask when the predicted regression line will cross a threshold value, which we set to a mean of pre-pandemic distances. We predict that a return to pre-pandemic cycles would be imminent for most pathogens (Figure 4B; see Supplementary Figure S9 for a zoomed out version). In addition, we also predict that many pathogens should have already returned to their pre-pandemic dynamics by the end of 2024; but these predictions contradict some of the observed pathogen dynamics. For example, we predict that both human metapneumovirus and RSV in Korea should have returned to their attractors by now, but the magnitude

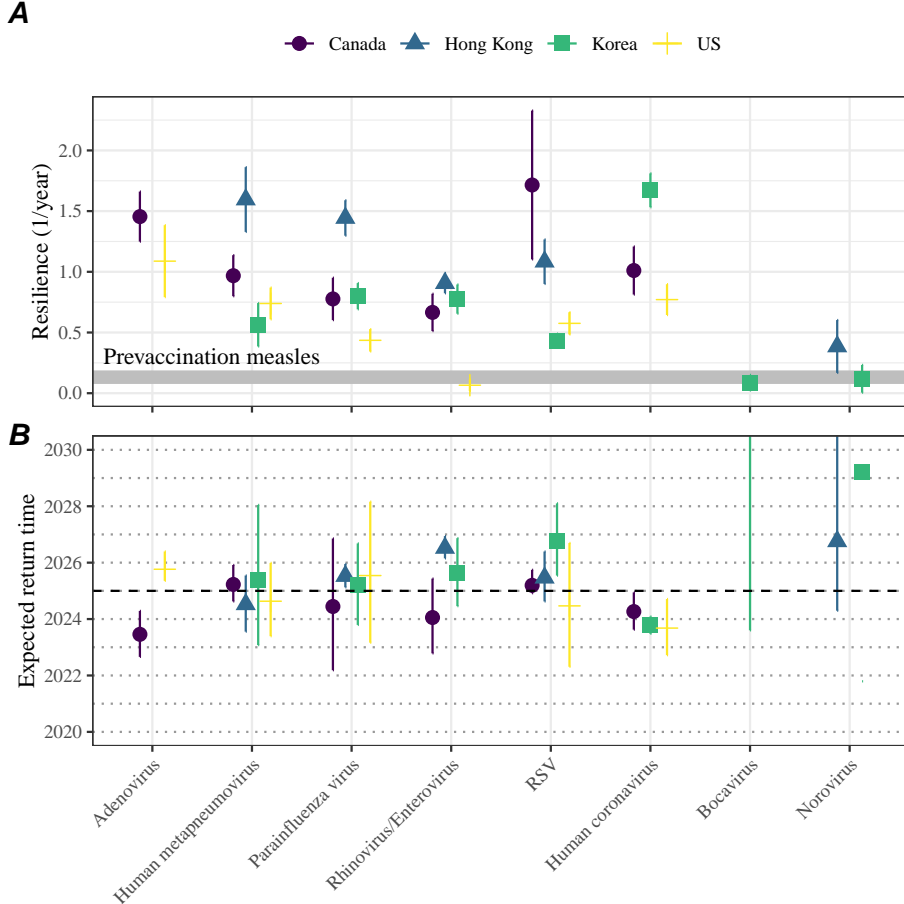


Figure 4: **Summary of resilience estimates.** (A) Estimated pathogen resilience. The gray horizontal line represents the intrinsic resilience of pre-vaccination measles dynamics. (B) Predicted timing of when each pathogen will return to their pre-pandemic cycles. The dashed line in panel B indicates the end of 2024 (current observation time). Error bars represent 95% confidence intervals.

and timing of recent epidemics are different from pre-pandemic patterns (Figure 1). These observations suggest the possibility that some common respiratory pathogens may have converged to different attractors.

In Supplementary Materials, we also consider using a lower threshold for the false nearest neighbor approach when determining the embedding dimension; this gives a higher embedding dimension. As explained earlier (Supplementary Figure S6), this gives a smoother distance-from-attractor time series (compare Supplementary Figure S10 with S8); this also requires us to use longer time series, which prevents us from estimating resilience for some pathogens. Overall, resulting estimates of pathogen resilience with higher embedding dimensions still fall between 0.3/year and 2.1/year for the most part (Supplementary Figure S11). A direct comparison

234 between two approaches (i.e., original estimate vs using higher dimensions) shows a
 235 strong consistency in resilience estimates (Supplementary Figure S12).

236 Susceptible host dynamics explain variation in pathogen 237 resilience

238 So far, we focused on quantifying pathogen resilience from the observed patterns of
 239 pathogen re-emergence following COVID-19 interventions. But what factors deter-
 240 mine how resilient a host-pathogen system is? Here, we use a standard Susceptible-
 241 Infected-Recovered-Susceptible (SIRS) model to show that susceptible host dynamics
 242 are the key determinants of pathogen resilience. To do so, we vary the basic reproduc-
 243 tion number \mathcal{R}_0 , which represents the average number of secondary infections caused
 244 by a newly infected individual in a fully susceptible population, and the duration of
 245 immunity and compute intrinsic resilience for each parameter.

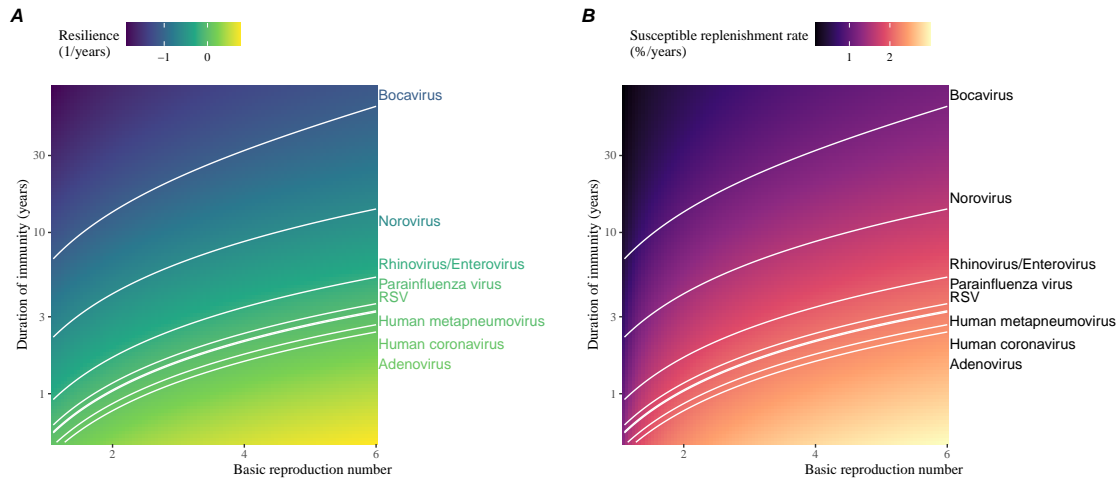


Figure 5: **Linking pathogen resilience to epidemiological parameters and susceptible host dynamics.** (A) The heat map represents intrinsic resilience as a function of the basic reproduction number \mathcal{R}_0 and the duration of immunity. (B) The heat map represents per-capita susceptible replenishment rate as a function of the basic reproduction number \mathcal{R}_0 and the duration of immunity. The standard SIRS model is used to compute intrinsic resilience and per-capita susceptible replenishment rate. Lines correspond to a set of parameters that are consistent with mean resilience estimates for each pathogen. Pathogens are ranked based on their mean resilience estimates, averaged across different countries.

246 We find an increase in \mathcal{R}_0 and a decrease in duration of immunity correspond
 247 to an increase in pathogen resilience (Figure 5A). These variations can be under-
 248 stood in terms of the susceptible host dynamics, where faster per-capita susceptible

249 replenishment rate causes the system to be more resilient (Figure 5B). This rate can
250 be expressed as a ratio between absolute rate at which new susceptibles enter the
251 population and the equilibrium number of susceptible individuals in the population,
252 \bar{S} . Therefore, both higher \mathcal{R}_0 and shorter duration of immunity can drive faster
253 per-capita susceptible replenishment rate (Figure 5B), especially because higher \mathcal{R}_0
254 leads to lower \bar{S} .

255 Finally, we can now rank different pathogens based on the average values of em-
256 pirical resilience, which allows us to determine a set of parameters that are consistent
257 with the estimated resilience (Figure 5A). Across all pathogens we consider, except
258 for bocavirus and norovirus, we estimate that the average duration of immunity is
259 likely to be short (< 6 years) across a plausible range of \mathcal{R}_0 . These rankings further
260 allow us to map each pathogen onto a set of parameters that are consistent with
261 its empirical resilience (Figure 5A) and obtain a plausible range of susceptible re-
262plenishment rates for each pathogen (Figure 5B). However, we note that there is no
263 one-to-one correspondence between susceptible replenishment rates and pathogen re-
264silience, leading to a wide uncertainty in the estimates for susceptible replenishment
265 rates (Figure 5B).

266 Discussion

267 The COVID-19 interventions have caused major disruptions to circulation patterns
268 of both respiratory and non-respiratory pathogens, adding challenges to predicting
269 their future dynamics [1, 2, 3, 4]. On the other hand, these interventions offer
270 large-scale natural experiments for understanding how different pathogens respond to
271 perturbations. In this study, we show that pathogen re-emergence patterns following
272 COVID-19 interventions can be characterized through the lens of ecological resilience.
273 Traditionally, ecological resilience measures how fast a system returns to a reference
274 state following a perturbation. In the context of respiratory pathogens, resilience
275 measures how fast epidemics return to their endemic cycles after interventions are
276 lifted.

277 We use an attractor reconstruction approach to quantify how distance from at-
278tractor changes over time for each pathogen [18]. We show that the resilience of
279 a host-pathogen system can be estimated by fitting a linear regression to a logged
280 distance-from-attractor time series. Overall, we estimate that the resilience for most
281 common respiratory pathogens ranges between 0.4/year and 1.8/year, which is 3–14
282 times more resilient than prevaccination measles, indicating potential challenges in
283 controlling common respiratory pathogens.

284 Our framework allows us to make phenomenological predictions about when each
285 pathogen will return to their endemic cycles. The ability to predict future epidemic
286 patterns from resilience estimates offers a new paradigm for epidemic forecasting.
287 While this approach cannot predict the exact timing of outbreaks or epidemic pat-
terns, it is nonetheless useful for predicting when epidemics will settle down to regular

289 cycles after a large perturbation, such as COVID-19 interventions.

290 Our analyses suggest a possibility that several pathogens may have converged
291 to different endemic cycles compared to their pre-pandemic epidemic patterns. Key
292 examples include human metapnuemovirus, RSV, and bocavirus in Korea as well as
293 RSV in Hong Kong. These changes may reflect changes in surveillance or actual shift
294 in the dynamics, caused by permanent changes in behavior or population-level immu-
295 nity. While it seems unlikely that permanent changes in behavior would only affect a
296 few pathogens and not others, we cannot rule out this possibility given heterogeneity
297 in the age of infection across different respiratory pathogens [SWP: CITE]. A shift
298 in population-level immunity is plausible, as the emergence of SARS-CoV-2 and ex-
299 tinction of influenza B/Yamagata likely caused major changes in immune landscapes;
300 interactions among co-circulating pathogens, such as cross immunity between RSV
301 and HMPV [22], may have also contributed to changes in population-level immu-
302 nity. However, we currently do not know how immunity, or lack thereof, from these
303 pathogens would affect infection from other pathogens. Future studies should use
304 detailed mechanistic models, coupled with behavioral and immunological data, to
305 test these hypotheses and better understand post-pandemic dynamics of endemic
306 pathogens.

307 We show that susceptible host dynamics shape pathogen resilience, where faster
308 replenishment of the susceptible population causes the pathogen to be more resilient.
309 For simplicity, we focus on waning immunity and birth as a main driver of the suscep-
310 tible host dynamics but other mechanisms can also contribute to the replenishment
311 of the susceptible population. In particular, pathogen evolution, especially the emer-
312 gence of antigenically novel strains, can cause effective waning of immunity in the
313 population; therefore, we hypothesize that faster rates of antigenic evolution can also
314 cause a pathogen to be more resilient. Future studies should explore the relationship
315 between the rate of evolution and resilience for antigenically evolving pathogens.

316 Quantifying pathogen resilience also offers novel approaches to validating population-
317 level epidemiological models. So far, the majority of model validation in epidemiology
318 is based on the ability of a model to reproduce the observed epidemic dynamics and
319 to predict future dynamics [23, 22, 24, 25, 26]. However, there can be plethora of
320 models that meet these criteria. For example, two major RSV models have been pro-
321 posed so far to explain biennial epidemic patterns: (1) a stage- and age-structured
322 model that allows for disease severity to vary with number of past infections and
323 age of infection [24] and (2) a pathogen-interaction model that accounts for cross
324 immunity between RSV and human metapnuemovirus [22]. Since both models can
325 accurately reproduce the observed epidemic patterns, standard criteria for model
326 validation do not allow us to distinguish between these two models from population-
327 level data alone. Instead, we can measure the empirical resilience of each model
328 by simulating various perturbations and compare them to estimates of empirical re-
329 siliience from data, using COVID-19 interventions as an opportunity. Future studies
330 should further investigate using pathogen resilience for validating epidemic models.

331 There are several limitations to our work. First of all, we did not extensively ex-

332 plore other approaches to reconstructing the attractor. Recent studies showed that
333 more sophisticated approaches, such as using non-uniform embedding, can provide
334 more robust reconstruction for noisy data [21]. In the context of causal inference,
335 choices about embedding can have major impact on the resulting inference [27]. Our
336 resilience estimates are likely overly confident given a lack of uncertainties in at-
337 tractor reconstruction as well as the simplicity of our statistical framework. Short
338 pre-pandemic time series also contributes to the crudeness of our estimates. Nonethe-
339 less, as illustrated in our sensitivity analyses (Supplementary Figure S6, S10–S12),
340 inferences about pathogen resilience appear to be robust to decisions about embed-
341 ding lags and dimensions—this is because tracking the rate at which the system
342 approaches the attractor is likely a much simpler problem than making inferences
343 about causal directionality. Our qualitative prediction that common respiratory
344 pathogens are more resilient than prevaccination measles is also likely to be robust
345 to these predictions, given how rapid many respiratory pathogens returned to their
346 original cycles following COVID-19 interventions.

347 Predicting the impact of anthropogenic changes on infectious disease dynam-
348 ics is a fundamental aim of infectious disease research in a rapidly changing world.
349 Our study illustrates that quantifying pathogen resilience can help us understand
350 how infectious disease pathogens respond to major perturbations caused by public
351 health interventions. More broadly, a detailed understanding of the determinants of
352 pathogen resilience may offer unique insights into pathogen persistence and control-
353 lability.

354 Materials and Methods

355 Data

356 We gathered time series on respiratory infections from four different countries: Canada,
357 Hong Kong, Korea, and United States (US). As a reference, we also included time
358 series data on norovirus infections for available countries—in contrast to respiratory
359 pathogens, we expect gastrointestinal viruses, such as norovirus, to be less affected
360 by COVID-19 intervention measures. For all time series, we rounded every year to
361 52 weeks by taking the average number of cases and tests between the 52nd and
362 53rd week. We also rescale all time series to account for changes in testing patterns,
363 which are then used for the actual analysis.

364 Weekly time series of respiratory infection cases in Canada comes from the Res-
365piratory Virus Detection Surveillance System, which collect data from select lab-
366 oratories across Canada. We extract the data from <https://www.canada.ca/en/public-health/services/surveillance/respiratory-virus-detections-canada.html>. To account for an increase in testing from 2013 to 2024, we calculate a 2 year
367 moving average for the number of tests for each pathogen, which we use as a proxy
368 for testing effort. Then, we divide the smoothed testing patterns by the smoothed
369 value at the final week such that the testing effort has a maximum of 1. We then
370 371

372 divide weekly cases by the testing effort to obtain a scaled case time series. A similar
373 approach was used earlier for the analysis of RSV time series in the US [24].

374 Weekly time series of respiratory infection cases in Hong Kong comes from the
375 Centre for Health Protection, Department of Health. We extract the data from
376 <https://www.chp.gov.hk/en/statistics/data/10/641/642/2274.html>. We also
377 apply the same scaling procedure to the time series as we did for Canada. For Hong
378 Kong, we only adjust for testing efforts up to the end of 2019 because there was a
379 major reduction in testing for common respiratory pathogens since 2020.

380 Weekly time series of acute respiratory infection cases in Korea comes from Ko-
381 rea Disease Control and Prevention Agency. We extract the data from <https://dportal.kdca.go.kr/pot/is/st/ari.do>. While we do not have information on
382 testing, the reported number of respiratory infections consistently increased from
383 2013 to the end of 2019, which we interpreted as changes in testing patterns. Since
384 we do not have testing numbers, we used the weekly sum of all acute respiratory vi-
385 ral infection cases as a proxy for testing, which were further smoothed with moving
386 averaged and scaled to have a maximum of 1. For Korea, we also only adjust for
387 testing efforts up to the end of 2019.

388 Finally, weekly time series of respiratory infection cases in the US comes from
389 the National Respiratory and Enteric Virus Surveillance System. In the US, there
390 has been a large increase in testing against some respiratory pathogens, especially
391 RSV, which could not be corrected for through simple scaling. Instead, we derive an
392 incidence proxy by multiplying the test positivity with influenza-like illness positivity,
393 which is taken from <https://gis.cdc.gov/grasp/fluview/fluportaldashboard.html>. This method of estimating an incidence proxy has been recently applied in
394 the analysis of seasonal coronaviruses [5] and Mycoplasma pneumoniae infections [4].
395 Detailed assumptions and justifications are provided in [28].

398 Estimating pathogen resilience

399 In order to measure pathogen resilience from surveillance data, we first reconstruct
400 the empirical pre-pandemic attractor of the system using Takens' embedding theorem
401 [18]. Specifically, for a given pathogen, we take the pre-pandemic (before 2020)
402 case time series $C(t)$ and reconstruct the attractor using delayed embedding with a
403 uniform delay of τ and dimension M :

$$X_{\tau,m}(t) = \langle \log(C(t) + 1), \log(C(t - \tau) + 1), \dots, \log(C(t - (M - 1)\tau) + 1) \rangle. \quad (2)$$

404 Here, the delay τ is determined by looking at the autocorrelation of the logged pre-
405 pandemic time series and asking when the autocorrelation crosses 0 for the first time
406 [21]; a typical delay for an annual outbreak is around 13 weeks.

407 Then, for a given delay τ , we determine the embedding dimension M using the
408 false nearest neighbors approach [20, 21]. To do so, we start with an embedding
409 dimension e and construct a set of points $A_{\tau,e} = \{X_{\tau,e}(t) | t < 2020\}$. Then, for
410 each point $X_{\tau,e}(t)$, we determine the nearest neighbor from the set $A_{\tau,e}$, which we

411 denote $X_{\tau,e}(t_{nn})$ for $t \neq t_{nn}$. Then, if the distance between these two points on $e+1$
 412 dimension, $D_{\tau,e+1}(t) = \|X_{\tau,e+1}(t_{nn}) - X_{\tau,e+1}(t)\|_2$, is larger than their distance on
 413 e dimension, $D_{\tau,e}(t) = \|X_{\tau,e}(t_{nn}) - X_{\tau,e}(t)\|_2$, these two points are deemed to be
 414 false nearest neighbors; specifically, we use a threshold R for the ratio between two
 415 distances $D_{\tau,e+1}(t)/D_{\tau,e}(t)$ to determine false nearest neighbors. In the main text,
 416 we determine embedding dimension based as the first dimension without any false
 417 nearest neighbors for $R = 10$. In Supplementary Materials, we impose $R = 5$ to select
 418 for higher dimensions. Once we determine the embedding lag τ and dimension M ,
 419 we apply the embedding to the entire time series and calculate the nearest neighbor
 420 distance against the attractor $A_{\tau,M}$ to obtain a time series of distance from attractor
 421 $D_{\tau,M}(t)$.

422 From a time series of distance from attractor, we estimate pathogen resilience
 423 by fitting a linear regression to an appropriate window. To automatically select
 424 the fitting window, we begin by smoothing the distance time series using locally
 425 estimated scatterplot smoothing (LOESS) to obtain $\hat{D}_{\tau,M}(t)$, where the smoothing
 426 is performed on a log scale and exponentiated afterwards. Then, we determine
 427 threshold values (T_{start} and T_{end}) for the smoothed distances and choose the fitting
 428 window based on when $\hat{D}_{\tau,M}(t)$ crosses these threshold values for the first time.
 429 These thresholds are determined by first calculating maximum distance,

$$\max \hat{D} = \max \hat{D}_{\tau,M}(t), \quad (3)$$

430 and mean pre-pandemic distance,

$$\hat{D}_{\text{mean}} = \frac{1}{N_{t < 2020}} \sum_{t < 2020} \hat{D}_{\tau,M}(t), \quad (4)$$

431 as a reference, and then dividing their ratios into 10 equal bins:

$$T_{\text{start}} = \hat{D}_{\text{mean}} \times \left(\frac{\max \hat{D}}{\hat{D}_{\text{mean}}} \right)^{9/10} \quad (5)$$

$$T_{\text{end}} = \hat{D}_{\text{mean}} \times \left(\frac{\max \hat{D}}{\hat{D}_{\text{mean}}} \right)^{1/10} \quad (6)$$

432 This allows us to discard the initial period during which the distance increases (from
 433 the introduction of intervention measures) and the final period during which the
 434 distance plateaus (as the system reaches an attractor). The fitting window is deter-
 435 mined based on when the smoothed distance $\hat{D}_{\tau,M}(t)$ crosses these threshold values
 436 for the first time; then, we fit a linear regression to logged (unsmoothed) distances
 437 $\log D_{\tau,M}(t)$ using that window.

438 Mathematical modeling

439 Throughout the paper, we use a series of mathematical models to illustrate the con-
 440 cept of pathogen resilience and to understand the determinants of pathogen resilience.

441 In general, the intrinsic resilience for a given system is given by the largest real part
 442 of the eigenvalues of the linearized system at endemic equilibrium. Here, we focus on
 443 the SIRS model and present the details of other models in Supplementary Materials.
 444 The SIRS (Susceptible-Infected-Recovered-Susceptible) model is the simplest model
 445 that allows for waning of immunity, where recovered (immune) individuals are as-
 446 sumed to become fully susceptible after an average of $1/\delta$ time period. The dynamics
 447 of the SIRS model is described by the following set of differential equations:

$$\frac{dS}{dt} = \mu - \beta(t)SI - \mu S + \delta R \quad (7)$$

$$\frac{dI}{dt} = \beta(t)SI - (\gamma + \mu)I \quad (8)$$

$$\frac{dR}{dt} = \gamma I - (\delta + \mu)R \quad (9)$$

(10)

448 where μ represents the birth/death rate, $\beta(t)$ represents the time-varying trans-
 449 mission rate, and γ represents the recovery rate. The basic reproduction number
 450 $\mathcal{R}_0 = \beta(t)/(\gamma + \mu)$ is defined as the average number of secondary infections caused
 451 by a single infected individual in a fully susceptible population and measures the
 452 intrinsic transmissibility of a pathogen.

453 When we first introduce the idea of pathogen resilience (Figure 2), we impose
 454 sinusoidal changes to the transmission rate to account for seasonal transmission:

$$\beta(t) = b_1(1 + \theta \cos(2\pi(t - \phi)))\alpha(t), \quad (11)$$

455 where b_1 represents the baseline transmission rate, θ represents the seasonal ampli-
 456 tude, and ϕ represents the seasonal offset term. Here, we also introduce an extra
 457 multiplicative term $\alpha(t)$ to account for the impact of COVID-19 interventions, where
 458 $\alpha(t) < 1$ indicates transmission reduction. Figure 2A and 2B are generated assuming
 459 $b_1 = 3 \times (365/7 + 1/50)/\text{years}$, $\theta = 0.2$, $\phi = 0$, $\mu = 1/50/\text{years}$, $\gamma = 365/7/\text{years}$, and
 460 $\delta = 1/2/\text{years}$. In Figure 2A, we impose a 50% transmission reduction for 6 months
 461 from 2020:

$$\alpha(t) = \begin{cases} 0.5 & 2020 \leq t < 2020.5 \\ 1 & \text{otherwise} \end{cases} \quad (12)$$

462 In Figure 2B, we impose a 50% transmission reduction for 6 months from 2020 and
 463 a permanent 10% reduction onward:

$$\alpha(t) = \begin{cases} 1 & t < 2020 \\ 0.5 & 2020 \leq t < 2020.5 \\ 0.9 & 2020.5 \leq t \end{cases} \quad (13)$$

464 In both scenarios, we simulate the SIRS model from the following initial conditions
 465 ($S(0) = 1/\mathcal{R}_0$, $I(0) = 1 \times 10^{-6}$, and $R(0) = 1 - S(0) - I(0)$) from 1900 until 2030.

466 To measure the empirical resilience of the SIR model (Figure 2C and 2F), we
 467 compute the normalized distance between post-intervention susceptible and logged
 468 infected proportions and their corresponding pre-intervention values at the same time
 469 of year:

$$\sqrt{\left(\frac{S(t) - S_{\text{pre}}(t)}{\sigma_S}\right)^2 + \left(\frac{\log I(t) - \log I_{\text{pre}}(t)}{\sigma_{\log I}}\right)^2}, \quad (14)$$

470 where σ_S and $\sigma_{\log I}$ represent the standard deviation in the pre-intervention suscep-
 471 tible and logged infected proportions. We normalize the differences in susceptible
 472 and logged infected proportions to allow both quantities to equally contribute to the
 473 changes in distance from attractor. In Supplementary Materials, we also compare
 474 the how the degree of seasonal transmission affects empirical resilience by varying
 475 θ from 0 to 0.4; when we assume no seasonality ($\theta = 0$), we do not normalize the
 476 distance because the standard deviation of pre-intervention dynamics are zero.

477 Finally, we use the SIRS model to understand how underlying epidemiological
 478 parameters affect pathogen resilience and link this relationship to underlying sus-
 479 ceptible host dynamics. For the simple SIRS model without seasonal transmission
 480 ($\theta = 0$), the intrinsic resilience corresponds to:

$$-\frac{\text{Re}(\lambda)}{2} = \frac{\delta + \beta I^* + \mu}{2}. \quad (15)$$

481 Here, I^* represents the prevalence values at endemic equilibrium:

$$I^* = \frac{(\delta + \mu)(\beta - (\gamma + \mu))}{\beta(\delta + \gamma + \mu)}. \quad (16)$$

482 The susceptible replenishment rate is given by:

$$S_{\text{replenish}} = \frac{\mu + \delta R}{S^*}, \quad (17)$$

483 where $S^* = 1/\mathcal{R}_0$ represents the equilibrium proportion of susceptible individuals.
 484 We vary the basic reproduction number \mathcal{R}_0 between 1.1 to 6 and the average duration
 485 of immunity $1/\delta$ between 2 to 80 years, and compute these two quantities. In doing
 486 so, we fix all other parameters: $\mu = 1/80/\text{years}$ and $\gamma = 365/7/\text{years}$.

487 **Supplementary Text**

488 **Resilience of a stage-structured system.**

489 In Figure 2G–I, we use a more realistic, stage-structured model to illustrate how
 490 transient phenomena can cause the system to slow down. Specifically, we use the
 491 stage-structured RSV model proposed by [24], which assumes that subsequent rein-
 492 fections cause an individual to become less susceptible and transmissible than previ-
 493 ous infections. The model dynamics can be described as follows:

$$\frac{dM}{dt} = \mu - (\omega + \mu)M \quad (S1)$$

$$\frac{dS_0}{dt} = \omega M - (\lambda(t) + \mu)S_0 \quad (S2)$$

$$\frac{dI_1}{dt} = \lambda(t)S_0 - (\gamma_1 + \mu)I_1 \quad (S3)$$

$$\frac{dS_1}{dt} = \gamma_1 I_1 - (\sigma_1 \lambda(t) + \mu)S_1 \quad (S4)$$

$$\frac{dI_2}{dt} = \sigma_1 \lambda(t)S_1 - (\gamma_2 + \mu)I_2 \quad (S5)$$

$$\frac{dS_2}{dt} = \gamma_2 I_2 - (\sigma_2 \lambda(t) + \mu)S_2 \quad (S6)$$

$$\frac{dI_3}{dt} = \sigma_2 \lambda(t)S_2 - (\gamma_3 + \mu)I_3 \quad (S7)$$

$$\frac{dS_3}{dt} = \gamma_3 I_3 - (\sigma_3 \lambda(t) + \mu)S_3 + \gamma_4 I_4 \quad (S8)$$

$$\frac{dI_4}{dt} = \sigma_3 \lambda(t)S_3 - (\gamma_4 + \mu)I_4 \quad (S9)$$

(S10)

494 where M represents the proportion of individuals who are maternally immune; S_i
 495 represents the proportion of individuals who are susceptible after i prior infections; I_i
 496 represents the proportion of individuals who are currently (re)-infected with their i -th
 497 infection; μ represents the birth and death rates; $1/\omega$ represents the mean duration
 498 of maternal immunity; $1/\gamma_i$ represents the mean duration of infection; $\lambda(t)$ represents
 499 the force of infection; and σ_i represents the reduction in susceptibility for reinfection.
 500 The force of infection is modeled using a sinusoidal function:

$$\beta(t) = b_1(1 + \theta \cos(2\pi(t - \phi)))\alpha(t) \quad (S11)$$

$$\lambda(t) = \beta(I_1 + \rho_1 I_2 + \rho_2(I_3 + I_4)), \quad (S12)$$

501 where b_1 represents the baseline transmission rate; θ represents the seasonal ampli-
 502 tude; ϕ represents the seasonal offset term; $\alpha(t)$ represents the intervention effect;
 503 and ρ_i represents the impact of immunity on transmission reduction. We use the

504 following parameters to simulate the impact of interventions on epidemic dynam-
 505 ics [24]: $b_1 = 9 \times (365/10 + 1/80)/\text{years}$, $\theta = 0.2$, $\phi = -0.1$, $\omega = 365/112/\text{years}$,
 506 $\gamma_1 = 365/10/\text{years}$, $\gamma_2 = 365/7/\text{years}$, $\gamma_3 = 365/5/\text{years}$, $\sigma_1 = 0.76$, $\sigma_2 = 0.6$,
 507 $\sigma_3 = 0.4$, $\rho_1 = 0.75$, $\rho_2 = 0.51$, and $\mu = 1/80/\text{years}$. We assume a 50% transmission
 508 reduction for 6 months from 2020:

$$\alpha(t) = \begin{cases} 0.5 & 2020 \leq t < 2020.5 \\ 1 & \text{otherwise} \end{cases} \quad (\text{S13})$$

509 The model is simulated from 1900 to 2030 using the following initial conditions:
 510 $M = 0$, $S_0 = 1/\mathcal{R}_0 - I_1$, $I_1 = 1 \times 10^{-6}$, $S_1 = 1 - 1/\mathcal{R}_0$, $I_2 = 0$, $S_2 = 0$, $I_3 = 0$,
 511 $S_3 = 0$, and $I_4 = 0$. For the phase plane analysis (Figure 2H) and distance analysis
 512 (Figure 2I), we rely on the average susceptibility,

$$\bar{S} = S_0 + \sigma_1 S_1 + \sigma_2 S_2 + \sigma_3 S_3, \quad (\text{S14})$$

513 and total prevalence,

$$I_{\text{total}} = I_1 + I_2 + I_3 + I_4. \quad (\text{S15})$$

514 These quantities are used to compute the normalized distance from the attractor, as
 515 described in the main text.

516 Resilience of a multistrain system.

517 We use a simple two-strain model to show that a multistrain host-pathogen system
 518 that is coupled through cross immunity can be described by a single resilience value.
 519 The model dynamics can be described as follows [22]:

$$\frac{dS}{dt} = \mu - \mu S - (\lambda_1 + \lambda_2)S + \rho_1 R_1 + \rho_2 R_2 \quad (\text{S16})$$

$$\frac{dI_1}{dt} = \lambda_1 S - (\gamma_1 + \mu)I_1 \quad (\text{S17})$$

$$\frac{dI_2}{dt} = \lambda_2 S - (\gamma_2 + \mu)I_2 \quad (\text{S18})$$

$$\frac{dR_1}{dt} = \gamma_1 I_1 - \lambda_2 \epsilon_{21} R_1 - \rho_1 R_1 + \rho_2 R - \mu R_1 \quad (\text{S19})$$

$$\frac{dR_2}{dt} = \gamma_2 I_2 - \lambda_1 \epsilon_{12} R_2 - \rho_2 R_2 + \rho_1 R - \mu R_2 \quad (\text{S20})$$

$$\frac{dJ_1}{dt} = \lambda_1 \epsilon_{12} R_2 - (\gamma_1 + \mu) J_1 \quad (\text{S21})$$

$$\frac{dJ_2}{dt} = \lambda_2 \epsilon_{21} R_1 - (\gamma_2 + \mu) J_2 \quad (\text{S22})$$

$$\frac{dR}{dt} = \gamma_1 J_1 + \gamma_2 J_2 - \rho_1 R - \rho_2 R - \mu R \quad (\text{S23})$$

520 where S represents the proportion of individuals who are fully susceptible to infections by both strains; I_1 represents the proportion of individuals who are infected with strain 1 without prior immunity; I_2 represents the proportion of individuals who are infected with strain 2 without prior immunity; R_1 represents the proportion of individuals who are fully immune against strain 1 and partially susceptible to reinfection by strain 2; R_2 represents the proportion of individuals who are fully immune against strain 2 and partially susceptible to reinfection by strain 1; J_1 represents the proportion of individuals who are infected with strain 1 with prior immunity against strain 2; J_2 represents the proportion of individuals who are infected with strain 2 with prior immunity against strain 1; R represents the proportion of individuals who are immune to infections from both strains; μ represents the birth/death rate; λ_1 and λ_2 represent the force of infection from strains 1 and 2, respectively; ρ_1 and ρ_2 represent the waning immunity rate; γ_1 and γ_2 represent the recovery rate; ϵ_{12} and ϵ_{21} represent the susceptibility to reinfection with strains 2 and 1, respectively, given prior immunity from infection with strains 1 and 2, respectively. The force of infection is modeled as follows:

$$\beta_1 = b_1(1 + \theta_1 \sin(2\pi(t - \phi_1)))\alpha(t) \quad (\text{S24})$$

$$\beta_2 = b_2(1 + \theta_2 \sin(2\pi(t - \phi_2)))\alpha(t) \quad (\text{S25})$$

$$\lambda_1 = \beta_1(I_1 + J_1) \quad (\text{S26})$$

$$\lambda_2 = \beta_2(I_2 + J_2) \quad (\text{S27})$$

536 In Supplementary Figures S2–S4, we assume the following parameters: $b_1 = 2 \times$
 537 $52/\text{years}$, $b_2 = 4 \times 52/\text{years}$, $\phi_1 = \phi_2 = 0$, $\epsilon_{12} = 0.9$, $\epsilon_{21} = 0.5$, $\gamma_1 = \gamma_2 = 52/\text{years}$,
 538 $\rho_1 = \rho_2 = 1/\text{years}$, and $\mu = 1/70/\text{years}$. For all simulations, we assume a 50%
 539 transmission reduction for 6 months from 2020:

$$\alpha(t) = \begin{cases} 0.5 & 2020 \leq t < 2020.5 \\ 1 & \text{otherwise} \end{cases} \quad (\text{S28})$$

540 The seasonal amplitude θ is varied from 0 to 0.4. All simulations are ran from 1900
 541 to 2030 from the following initial conditions: $S(0) = 1 - 2 \times 10^{-6}$, $I_1(0) = 1 \times 10^{-6}$,
 542 $I_2(0) = 1 \times 10^{-6}$, $R_1(0) = 0$, $R_2(0) = 0$, $J_1(0) = 0$, $J_2(0) = 0$, and $R(0) = 0$.

543 For this, we consider three different scenarios for measuring pathogen resilience:
 544 (1) we only have information about strain 1, (2) we only have information about
 545 strain 2, and (3) we are unable to distinguish the differences between strains. In
 546 the first two scenarios (see panels A–C for strain 1 and panels D–F for strain 2), we
 547 consider the dynamics of average susceptibility for each strain and total prevalence:

$$\bar{S}_1 = S + \epsilon_{12}R_2 \quad (\text{S29})$$

$$\hat{I}_1 = I_1 + J_1 \quad (\text{S30})$$

$$\bar{S}_2 = S + \epsilon_{21}R_1 \quad (\text{S31})$$

$$\hat{I}_2 = I_2 + J_2 \quad (\text{S32})$$

548 In the third scenario (panels G–I), we consider the dynamics of total susceptible and
549 infected population:

$$\hat{S} = S + R_2 + R_1 \quad (\text{S33})$$

$$\hat{I} = I_1 + J_1 + I_2 + J_2 \quad (\text{S34})$$

$$(\text{S35})$$

550 These quantities are used to compute the normalized distance from the attractor, as
551 described in the main text.

552 Estimating intrinsic resilience using mechanistic model

553 We test whether we can reliably estimate the intrinsic resilience of a system by fitting
554 a mechanistic model. Specifically, we simulate case time series from stochastic SIRS
555 and two-strain models and fit a simple, deterministic SIRS model using a Bayesian
556 framework.

557 First, we describe the simulation set up. The stochastic SIRS model can be
558 written as follows:

$$\beta(t) = \mathcal{R}_0 \left(1 + \theta \cos \left(\frac{2\pi t}{364} \right) \right) \alpha(t)(1 - \exp(-\gamma)) \quad (\text{S36})$$

$$\text{FOI}(t) = \beta(t)I(t - \Delta t)/N \quad (\text{S37})$$

$$B(t) \sim \text{Poisson}(\mu N) \quad (\text{S38})$$

$$\Delta S(t) \sim \text{Binom}(S(t - \Delta t), 1 - \exp(-(\text{FOI}(t) + \mu)\Delta t)) \quad (\text{S39})$$

$$N_{SI}(t) \sim \text{Binom}\left(\Delta S(t), \frac{\text{FOI}(t)}{\text{FOI}(t) + \mu}\right) \quad (\text{S40})$$

$$\Delta I(t) \sim \text{Binom}(I(t - \Delta t), 1 - \exp(-(\gamma + \mu)\Delta t)) \quad (\text{S41})$$

$$N_{IR}(t) \sim \text{Binom}\left(\Delta I(t), \frac{\gamma}{\gamma + \mu}\right) \quad (\text{S42})$$

$$\Delta R(t) \sim \text{Binom}(R(t - \Delta t), 1 - \exp(-(\delta + \mu)\Delta t)) \quad (\text{S43})$$

$$N_{RS}(t) \sim \text{Binom}\left(\Delta R(t), \frac{\delta}{\delta + \mu}\right) \quad (\text{S44})$$

$$S(t) = S(t - \Delta t) + N_{RS}(t) + B(t) - \Delta S(t) \quad (\text{S45})$$

$$I(t) = I(t - \Delta t) + N_{SI}(t) - \Delta I(t) \quad (\text{S46})$$

$$R(t) = R(t - \Delta t) + N_{IR}(t) - \Delta R(t) \quad (\text{S47})$$

559 where FOI represent the force of infection; N_{ij} represent the number of individuals
560 moving from compartment i to j on a given day; and $B(t)$ represents the number
561 of new births. We simulate the model on a daily scale—assuming 364 days in a
562 year so that it can be evenly grouped into 52 weeks—with the following parameters:
563 $\mathcal{R}_0 = 3$, $\theta = 0.1$, $\gamma = 1/7/\text{days}$, $\delta = 1/(364 \times 2)/\text{days}$, $\mu = 1/(364 \times 50)/\text{days}$, and

⁵⁶⁴ $N = 1 \times 10^8$. The model is simulated from 1900 to 2030 assuming $S(0) = N/3$,
⁵⁶⁵ $I(0) = 100$, and $R(0) = N - S(0) - I(0)$. The observed incidence from the model is
⁵⁶⁶ then simulated as follows:

$$C(t) = \text{Beta} - \text{Binom}(N_{SI}(t), \rho, k), \quad (\text{S48})$$

⁵⁶⁷ where ρ represents the reporting probability and k represents the overdispersion pa-
⁵⁶⁸ rameter of beta-binomial distribution. We assume $\rho = 0.002$ (i.e., 0.2% probability)
⁵⁶⁹ and $k = 1000$.

⁵⁷⁰ The stochastic two-strain model can be written as follows:

$$\beta_1(t) = b_1 \left(1 + \theta_1 \cos \left(\frac{2\pi(t - \phi_1)}{364} \right) \right) \alpha(t) \quad (\text{S49})$$

$$\beta_2(t) = b_2 \left(1 + \theta_2 \cos \left(\frac{2\pi(t - \phi_2)}{364} \right) \right) \alpha(t) \quad (\text{S50})$$

$$\text{FOI}_1(t) = \beta_1(t)(I_1(t - \Delta t) + J_1(t - \Delta t))/N \quad (\text{S51})$$

$$\text{FOI}_2(t) = \beta_2(t)(I_2(t - \Delta t) + J_2(t - \Delta t))/N \quad (\text{S52})$$

$$B(t) \sim \text{Poisson}(\mu N) \quad (\text{S53})$$

$$\Delta S(t) \sim \text{Binom}(S(t - \Delta t), 1 - \exp(-(\text{FOI}_1(t) + \text{FOI}_2(t) + \mu)\Delta t)) \quad (\text{S54})$$

$$N_{SI_1}(t) \sim \text{Binom}\left(\Delta S(t), \frac{\text{FOI}_1(t)}{\text{FOI}_1(t) + \text{FOI}_2(t) + \mu}\right) \quad (\text{S55})$$

$$N_{SI_2}(t) \sim \text{Binom}\left(\Delta S(t), \frac{\text{FOI}_2(t)}{\text{FOI}_1(t) + \text{FOI}_2(t) + \mu}\right) \quad (\text{S56})$$

$$\Delta I_1(t) \sim \text{Binom}(I_1(t - \Delta t), 1 - \exp(-(\gamma_1 + \mu)\Delta t)) \quad (\text{S57})$$

$$N_{I_1 R_1}(t) \sim \text{Binom}\left(\Delta I_1(t), \frac{\gamma_1}{\gamma_1 + \mu}\right) \quad (\text{S58})$$

$$\Delta I_2(t) \sim \text{Binom}(I_2(t - \Delta t), 1 - \exp(-(\gamma_2 + \mu)\Delta t)) \quad (\text{S59})$$

$$N_{I_2 R_2}(t) \sim \text{Binom}\left(\Delta I_2(t), \frac{\gamma_2}{\gamma_2 + \mu}\right) \quad (\text{S60})$$

$$\Delta R_1(t) \sim \text{Binom}(R_1(t - \Delta t), 1 - \exp(-(\epsilon_{21}\text{FOI}_2(t) + \rho_1 + \mu)\Delta t)) \quad (\text{S61})$$

$$N_{R_1 S}(t) \sim \text{Binom}\left(\Delta R_1(t), \frac{\rho_1}{\epsilon_{21}\text{FOI}_2(t) + \rho_1 + \mu}\right) \quad (\text{S62})$$

$$N_{R_1 J_2}(t) \sim \text{Binom}\left(\Delta R_1(t), \frac{\epsilon_{21}\text{FOI}_2(t)}{\epsilon_{21}\text{FOI}_2(t) + \rho_1 + \mu}\right) \quad (\text{S63})$$

$$\Delta R_2(t) \sim \text{Binom}(R_2(t - \Delta t), 1 - \exp(-(\epsilon_{12}\text{FOI}_1(t) + \rho_2 + \mu)\Delta t)) \quad (\text{S64})$$

$$N_{R_2 S}(t) \sim \text{Binom}\left(\Delta R_2(t), \frac{\rho_2}{\epsilon_{12}\text{FOI}_1(t) + \rho_2 + \mu}\right) \quad (\text{S65})$$

$$N_{R_2 J_1}(t) \sim \text{Binom}\left(\Delta R_2(t), \frac{\epsilon_{12}\text{FOI}_1(t)}{\epsilon_{12}\text{FOI}_1(t) + \rho_2 + \mu}\right) \quad (\text{S66})$$

$$\Delta J_1(t) \sim \text{Binom}(J_1(t - \Delta t), 1 - \exp(-(\gamma_1 + \mu)\Delta t)) \quad (\text{S67})$$

$$N_{J_1R}(t) \sim \text{Binom}\left(\Delta J_1(t), \frac{\gamma_1}{\gamma_1 + \mu}\right) \quad (\text{S68})$$

$$\Delta J_2(t) \sim \text{Binom}(J_2(t - \Delta t), 1 - \exp(-(\gamma_2 + \mu)\Delta t)) \quad (\text{S69})$$

$$N_{J_2R}(t) \sim \text{Binom}\left(\Delta J_2(t), \frac{\gamma_2}{\gamma_2 + \mu}\right) \quad (\text{S70})$$

$$\Delta R(t) \sim \text{Binom}(R(t - \Delta t), 1 - \exp(-(\rho_1 + \rho_2 + \mu)\Delta t)) \quad (\text{S71})$$

$$N_{RR_1}(t) \sim \text{Binom}\left(\Delta R(t), \frac{\rho_1}{\rho_1 + \rho_2 + \mu}\right) \quad (\text{S72})$$

$$N_{RR_2}(t) \sim \text{Binom}\left(\Delta R(t), \frac{\rho_2}{\rho_1 + \rho_2 + \mu}\right) \quad (\text{S73})$$

$$S(t) = S(t - \Delta t) - \Delta S(t) + B(t) + N_{R_1S}(t) + N_{R_2S}(t) \quad (\text{S74})$$

$$I_1(t) = I_1(t - \Delta t) - \Delta I_1(t) + N_{SI_1}(t) \quad (\text{S75})$$

$$I_2(t) = I_2(t - \Delta t) - \Delta I_2(t) + N_{SI_2}(t) \quad (\text{S76})$$

$$R_1(t) = R_1(t - \Delta t) - \Delta R_1(t) + N_{I_1R_1}(t) + N_{RR_1}(t) \quad (\text{S77})$$

$$R_2(t) = R_2(t - \Delta t) - \Delta R_2(t) + N_{I_2R_2}(t) + N_{RR_2}(t) \quad (\text{S78})$$

$$J_1(t) = J_1(t - \Delta t) - \Delta J_1(t) + N_{R_2J_1}(t) \quad (\text{S79})$$

$$J_2(t) = J_2(t - \Delta t) - \Delta J_2(t) + N_{R_1J_2}(t) \quad (\text{S80})$$

$$R(t) = R(t - \Delta t) - \Delta R(t) + N_{J_1R}(t) + N_{J_2R}(t) \quad (\text{S81})$$

571 We simulate the model on a daily scale with previously estimated parameters for the
 572 RSV-HMPV interaction [22]: $b_1 = 1.7/\text{weeks}$, $b_2 = 1.95/\text{weeks}$, $\theta_1 = 0.4$, $\theta_2 = 0.3$,
 573 $\phi_1 = 0.005 \times 7/364$, $\phi_2 = 4.99 \times 7/364$, $\epsilon_{12} = 0.92$, $\epsilon_{21} = 0.45$, $\gamma_1 = 1/10/\text{days}$,
 574 $\gamma_2 = 1/10/\text{days}$, $\rho_1 = 1/364/\text{days}$, $\rho_2 = 1/364/\text{days}$, $\mu = 1/(70 \times 364)/\text{days}$, and
 575 $N = 1 \times 10^8$. The model is simulated from 1900 to 2030 assuming $S(0) = N - 200$,
 576 $I_1(0) = 100$, $I_2(0) = 100$, $R_1(0) = 0$, $R_2(0) = 0$, $J_1(0) = 0$, $J_2(0) = 0$, and $R(0) = 0$.
 577 The observed incidence for each strain is then simulated as follows:

$$C_1(t) = \text{Beta} - \text{Binom}(N_{SI_1}(t) + N_{R_2J_1}, \rho, k), \quad (\text{S82})$$

$$C_2(t) = \text{Beta} - \text{Binom}(N_{SI_2}(t) + N_{R_1J_2}, \rho, k), \quad (\text{S83})$$

578 where ρ represents the reporting probability and k represents the overdispersion pa-
 579 rameter of beta-binomial distribution. We assume $\rho = 0.002$ (i.e., 0.2% probability)
 580 and $k = 500$. We also consider the total incidence: $C_{\text{total}}(t) = C_1(t) + C_2(t)$.

581 For both models, we consider a more realistic challenges in intervention effects
 582 $\alpha(t)$ to challenge our ability to estimate the intervention effects. Thus, we assume
 583 a 40% transmission reduction for 3 months from March 2020, followed by a 10%
 584 transmission reduction for 6 months, 20% transmission reduction for 3 months, and

585 a final return to normal levels:

$$\alpha(t) = \begin{cases} 1 & t < 2020.25 \\ 0.6 & 2020.25 \leq t < 2020.5 \\ 0.9 & 2020.5 \leq t < 2021 \\ 0.8 & 2021 \leq t < 2021.25 \\ 1 & 2021.25 \leq t \end{cases}. \quad (\text{S84})$$

586 For all simulations, we truncate the time series from the beginning of 2014 to the
587 end of 2023 and aggregate them into weekly cases.

588 To infer intrinsic resilience from time series, we fit a simple discrete time, deter-
589 ministic SIRS model [4]:

$$\Delta t = 1 \text{ week} \quad (\text{S85})$$

$$\text{FOI}(t) = \beta(t)(I(t - \Delta t) + \omega)/N \quad (\text{S86})$$

$$\Delta S(t) = [1 - \exp(-(\text{FOI}(t) + \mu)\Delta t)] S(t - \Delta t) \quad (\text{S87})$$

$$N_{SI}(t) = \frac{\text{FOI}(t)\Delta S(t)}{\text{FOI}(t) + \mu} \quad (\text{S88})$$

$$\Delta I(t) = [1 - \exp(-(\gamma + \mu)\Delta t)] I(t - \Delta t) \quad (\text{S89})$$

$$N_{IR}(t) = \frac{\gamma \Delta I(t)}{\gamma + \mu} \quad (\text{S90})$$

$$\Delta R(t) = [1 - \exp(-(\nu + \mu)\Delta t)] R(t - \Delta t) \quad (\text{S91})$$

$$N_{RS}(t) = \frac{\nu \Delta R(t)}{\nu + \mu} \quad (\text{S92})$$

$$S(t) = S(t - \Delta t) + \mu S - \Delta S(t) + N_{RS}(t) \quad (\text{S93})$$

$$I(t) = I(t - \Delta t) - \Delta I(t) + N_{SI}(t) \quad (\text{S94})$$

$$R(t) = R(t - \Delta t) - \Delta R(t) + N_{IR}(t) \quad (\text{S95})$$

590 where we include an extra term ω to account for external infections. Although actual
591 simulations do not include any external infections, we found that including this term
592 generally helped with model convergence in previous analyses [4]. The transmission
593 rate is divided into a seasonal term $\beta_{\text{seas}}(t)$ (repeated every year) and intervention
594 term $\alpha(t)$, which are estimated jointly:

$$\beta(t) = \beta_{\text{seas}}(t)\alpha(t), \quad (\text{S96})$$

595 where $\alpha < 1$ corresponds to reduction in transmission due to intervention effects. To
596 constrain the smoothness of $\beta_{\text{seas}}(t)$, we impose cyclic, random-walk priors:

$$\beta_{\text{seas}}(t) \sim \text{Normal}(\beta_{\text{seas}}(t - 1), \sigma) \quad t = 2 \dots 52 \quad (\text{S97})$$

$$\beta_{\text{seas}}(1) \sim \text{Normal}(\beta_{\text{seas}}(52), \sigma) \quad (\text{S98})$$

597 [SWP: I noticed that I forgot to put a prior on σ so need to re-do this but won't
 598 change the results.] We fix $\alpha(t) = 1$ for all $t < 2020$ and estimate α assuming a
 599 normal prior:

$$\alpha \sim \text{Normal}(1, 0.25). \quad (\text{S99})$$

600 We assume weakly informative priors on ω and τ :

$$\omega \sim \text{Normal}(0, 200) \tau \sim \text{Normal}(104, 26) \quad (\text{S100})$$

601 We assume that the true birth/death rates, population sizes, and recovery rates are
 602 known. We note, however, that assuming $\gamma = 1/\text{week}$ actually correspond to a
 603 mean infectious period of 1.6 weeks, which is much longer than the true value; this
 604 approximation allows us to test whether we can still robustly estimate the intrinsic
 605 resilience given parameters mis-specification. Initial conditions are estimated with
 606 following priors:

$$S(0) = Ns(0) \quad (\text{S101})$$

$$I(0) = Ni(0) \quad (\text{S102})$$

$$s(0) \sim \text{Uniform}(0, 1) \quad (\text{S103})$$

$$i(0) \sim \text{Half-Normal}(0, 0.001) \quad (\text{S104})$$

607 Finally, the Observation model is specified as follows:

$$\text{Cases}(t) \sim \text{Negative-Binomial}(\rho N_{SI}(t), \phi) \quad (\text{S105})$$

$$\rho \sim \text{Half-Normal}(0, 0.02) \quad (\text{S106})$$

$$\phi \sim \text{Half-Normal}(0, 10) \quad (\text{S107})$$

608 where ρ represents the reporting probability and ϕ represents the negative binomial
 609 overdispersion parameter.

610 The model is fitted to four separate time series: (1) incidence time series from
 611 the SIRS model, (2) incidence time series for strain 1 from the two-strain model,
 612 (3) incidence time series for strain 2 from the two-strain model, and (4) combined
 613 incidence time series for strains 1 and 2 from the two-strain model. The model was
 614 fitted using rstan [29, 30]. The resulting posterior distribution was used to calculate
 615 the intrinsic resilience of the seasonally unforced system with the same parameters;
 616 eigenvalues of the discrete-time SIR model were computed by numerically finding
 617 the equilibrium and calculating the Jacobian matrix.

618 **Validations for window-selection criteria**

619 We use stochastic SIRS simulations to validate the window-selection criteria that we
 620 use for the linear regression for estimating empirical resilience. For each simulation,
 621 we begin by generating a random intervention $\alpha(t)$ from random set of parameters.
 622 First, we draw the duration of intervention τ_{np}^* from a uniform distribution between

623 0.5 and 3.5 years. Then, we draw independent normal variables z_i of length $\lfloor 364\tau_{\text{npi}} \rfloor$
 624 with a standard deviation of 0.02 and take a reverse cumulative sum to obtain a
 625 realistic shape for the intervention:

$$x_n = 1 + \sum_{i=n}^{\lfloor 364\tau_{\text{npi}} \rfloor} z_i, \quad n = 1, \dots, \lfloor 364\tau_{\text{npi}} \rfloor. \quad (\text{S108})$$

626 We repeat this random generation process until less than 10% of x_n exceeds 1. Then,
 627 we set any values that are above 1 or below 0 as 1 and 0, respectively. Then, we
 628 randomly draw the minimum transmission during intervention α_{\min} from a uniform
 629 distribution between 0.5 and 0.7 and scale x_n to have a minimum of α_{\min} :

$$x_{\text{scale},n} = \alpha_{\min} + (1 - \alpha_{\min}) \times \frac{x_n - \min x_n}{1 - \min x_n}. \quad (\text{S109})$$

630 This allows us to simulate a realistically shaped interventions:

$$\alpha(t) = \begin{cases} 1 & t < 2020 \\ x_{\text{scale},364(t-2020)} & 2020 \leq t < 2020 + \tau_{\text{npi}} \\ 1 & \tau_{\text{npi}} \leq t \end{cases}. \quad (\text{S110})$$

631 Given this intervention function, we draw \mathcal{R}_0 from a uniform distribution between 1.5
 632 and 3 and the mean duration of immunity $1/\delta$ from a uniform distribution between
 633 0.5 and 2. Then, we simulate the stochastic SIRS model from $S(0) = 10^8/\mathcal{R}_0$ and
 634 $I(0) = 100$ from 1990 to 2025 and truncate the time series to 2014–2025; if the
 635 epidemic becomes extinct before the end of simulation, we discard that simulation
 636 and start over from the intervention generation step. We then apply the window
 637 selection criteria described in the main text to compute the empirical resilience and
 638 compare it against the intrinsic resilience of the seasonally unforced system. We also
 639 compare this with the naive approach that uses the entire distance-from-attractor
 640 time series, starting from the maximum distance. We repeat this procedure 500
 641 times and quantify the correlation between empirical and intrinsic resilience estimates
 642 across two approaches.

Supplementary Figures

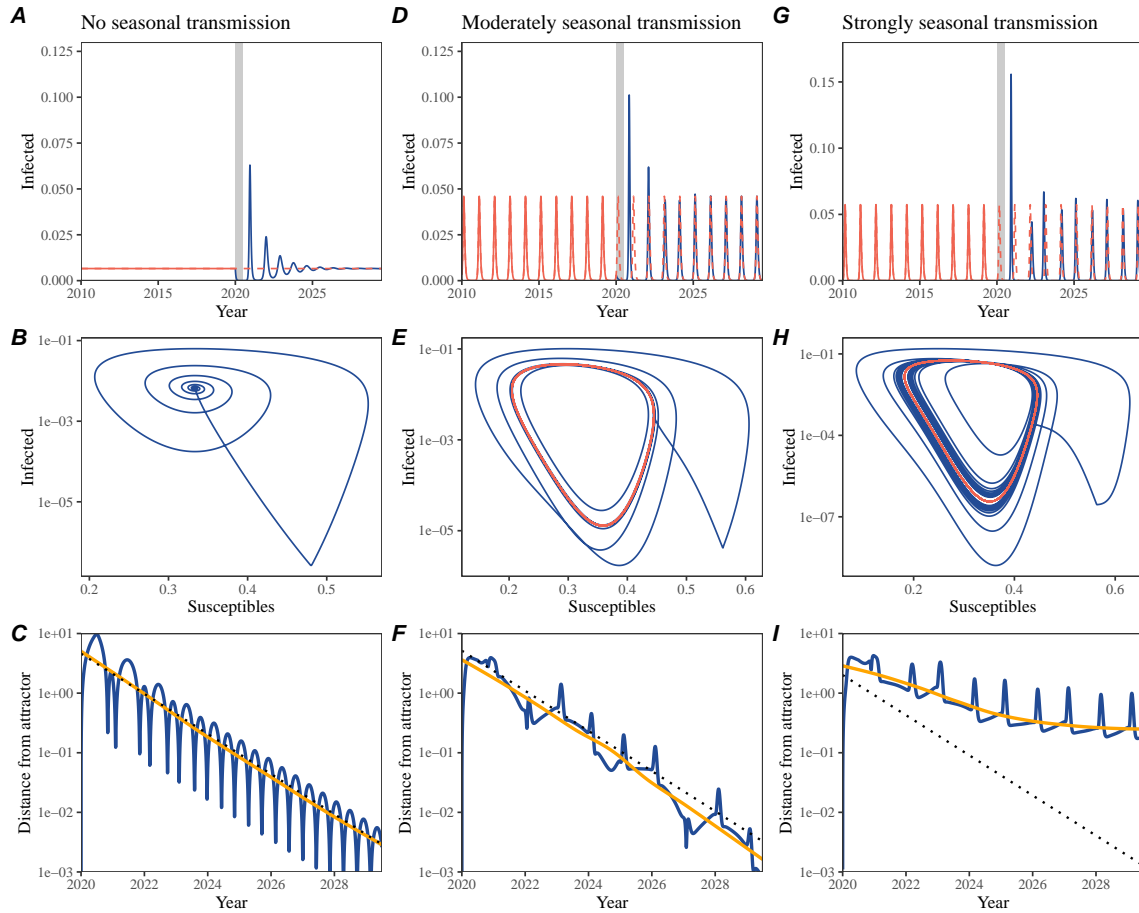


Figure S1: Impact of seasonal transmission on pathogen resilience. (A, D, G) Simulated epidemic trajectories using the SIRS model without seasonal forcing (A), with seasonal forcing of amplitude of 0.2 (D), and with seasonal forcing of amplitude of 0.2 (G). Red and blue solid lines represent epidemic dynamics before and after interventions are introduced, respectively. Red dashed lines represent counterfactual epidemic dynamics in the absence of interventions. Gray regions indicate the duration of interventions. (B, E, H) Phase plane representation of the corresponding model. Red and blue solid lines represent epidemic trajectories on an SI phase plane before and after interventions are introduced, respectively. (C, F, I) Changes in logged distance from attractor over time. Blue lines represent the logged distance from attractor. Orange lines represent the locally estimated scatterplot smoothing (LOESS) fits to the logged distance from attractor. Dotted lines are superimposed as a comparison to have the same slope as the intrinsic resilience of the seasonally unforced system.

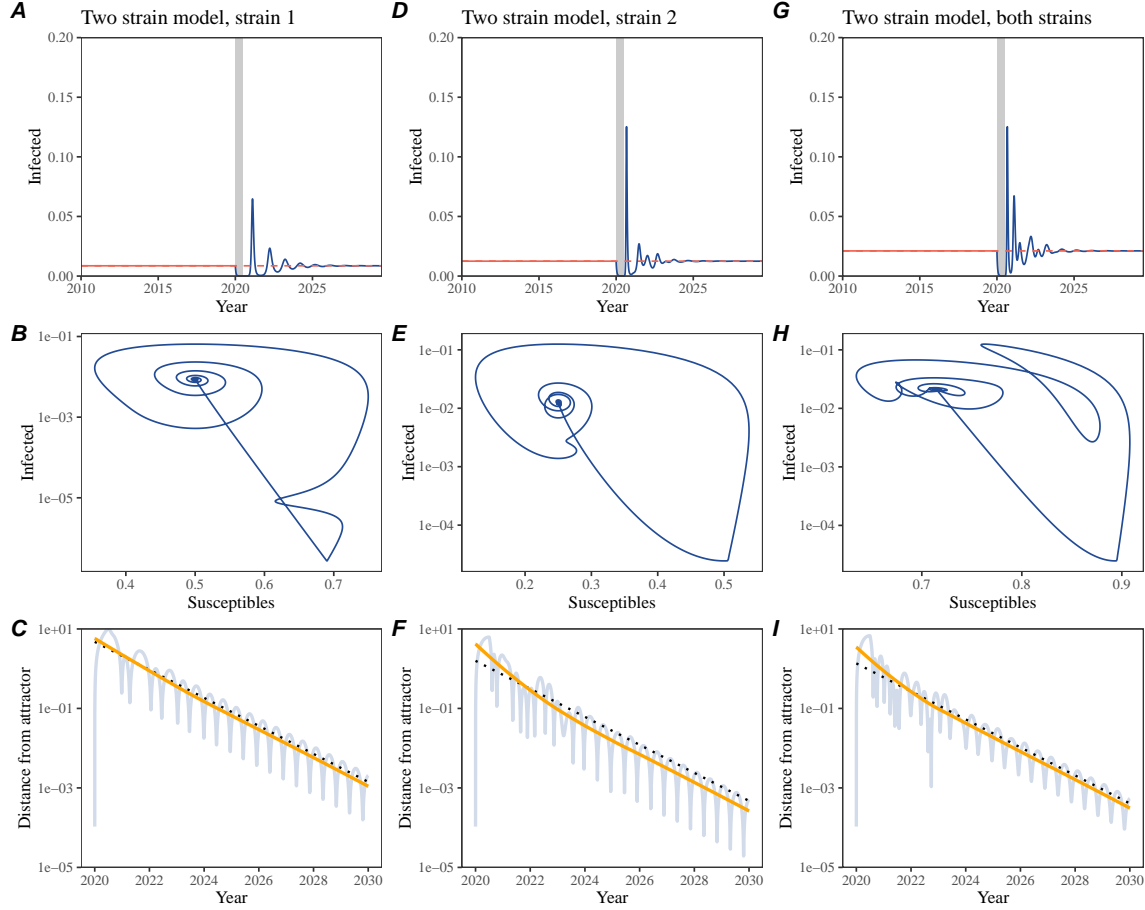


Figure S2: Conceptual framework for measuring pathogen resilience following NPIs for a multi-strain system without seasonal forcing. (A, D, G) Simulated epidemic trajectories using a multi-strain system without seasonal forcing. Red and blue solid lines represent epidemic dynamics before and after interventions are introduced, respectively. Red dashed lines represent counterfactual epidemic dynamics in the absence of interventions. Gray regions indicate the duration of interventions. (B, E, H) Phase plane representation of the corresponding model. Red and blue solid lines represent epidemic trajectories on an SI phase plane before and after interventions are introduced, respectively. (C, F, I) Changes in logged distance from attractor over time. Blue lines represent the logged distance from attractor. Orange lines represent the locally estimated scatterplot smoothing (LOESS) fits to the logged distance from attractor. Dotted lines are superimposed as a comparison to have the same slope as the intrinsic resilience of the seasonally unforced system.

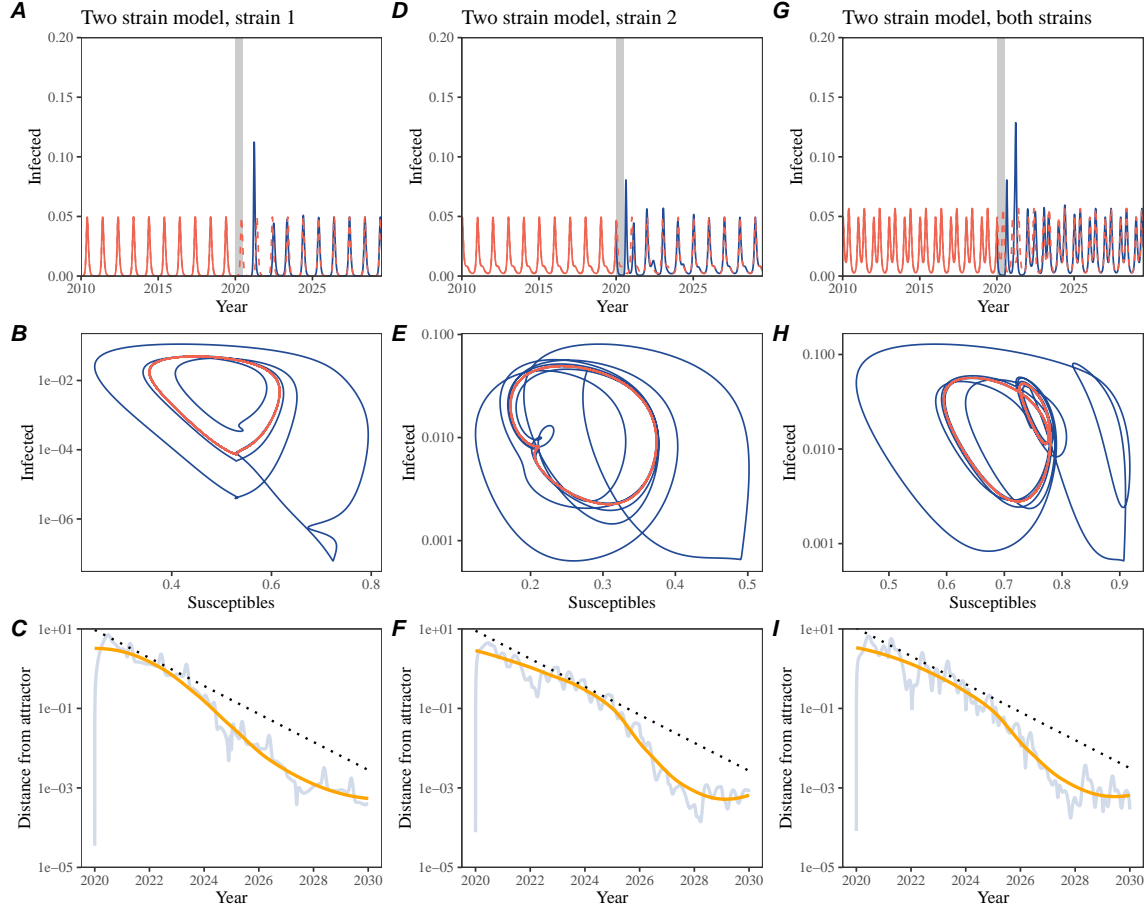


Figure S3: Conceptual framework for measuring pathogen resilience following NPIs for a multi-strain system with seasonal forcing. (A, D, G) Simulated epidemic trajectories using a multi-strain system with seasonal forcing (amplitude of 0.2). Red and blue solid lines represent epidemic dynamics before and after interventions are introduced, respectively. Red dashed lines represent counterfactual epidemic dynamics in the absence of interventions. Gray regions indicate the duration of interventions. (B, E, H) Phase plane representation of the corresponding model. Red and blue solid lines represent epidemic trajectories on an SI phase plane before and after interventions are introduced, respectively. (C, F, I) Changes in logged distance from attractor over time. Blue lines represent the logged distance from attractor. Orange lines represent the locally estimated scatterplot smoothing (LOESS) fits to the logged distance from attractor. Dotted lines are superimposed as a comparison to have the same slope as the intrinsic resilience of the seasonally unforced system.

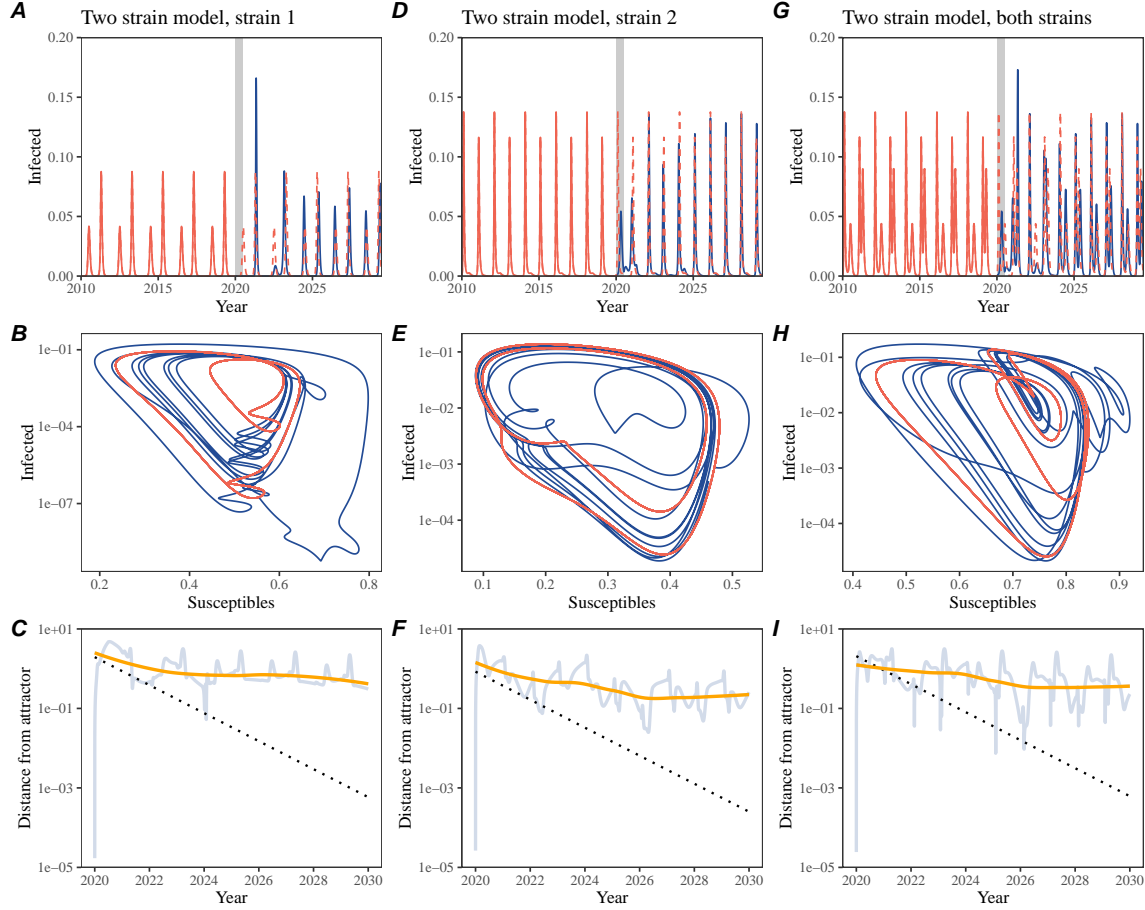


Figure S4: Conceptual framework for measuring pathogen resilience following NPIs for a multi-strain system with strong seasonal forcing. (A, D, G) Simulated epidemic trajectories using a multi-strain system with seasonal forcing (amplitude of 0.4). Red and blue solid lines represent epidemic dynamics before and after interventions are introduced, respectively. Red dashed lines represent counterfactual epidemic dynamics in the absence of interventions. Gray regions indicate the duration of interventions. (B, E, H) Phase plane representation of the corresponding model. Red and blue solid lines represent epidemic trajectories on an SI phase plane before and after interventions are introduced, respectively. (C, F, I) Changes in logged distance from attractor over time. Blue lines represent the logged distance from attractor. Orange lines represent the locally estimated scatterplot smoothing (LOESS) fits to the logged distance from attractor. Dotted lines are superimposed as a comparison to have the same slope as the intrinsic resilience of the seasonally unforced system.

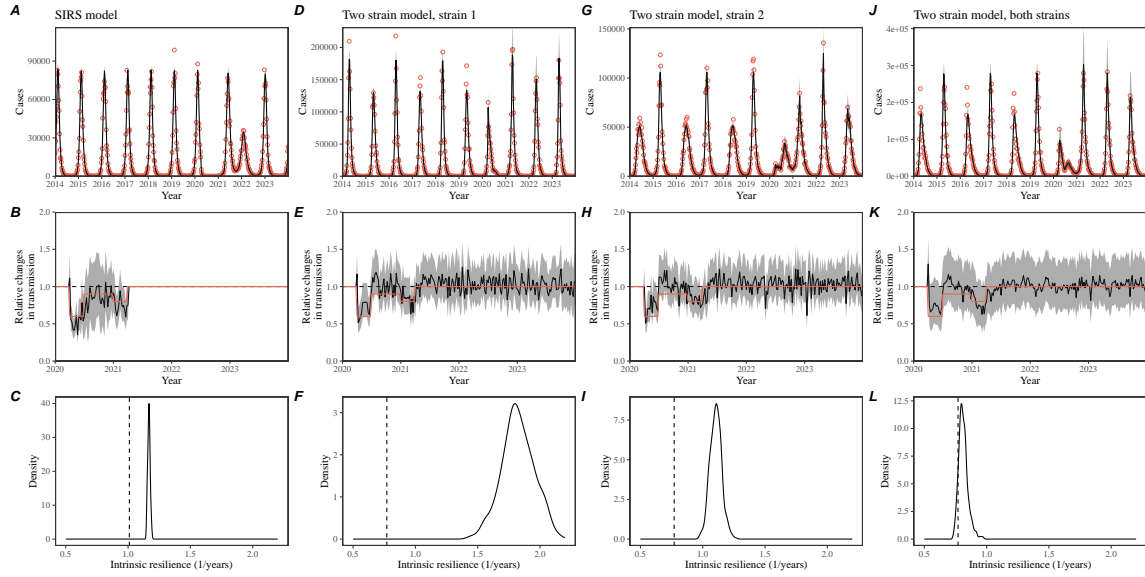


Figure S5: Mechanistic model fits to simulated data and inferred intrinsic resilience. (A, D, G, J) Simulated case time series from corresponding models (red) and SIRS model fits (black). (B, E, H, K) Assumed changes in transmission due to COVID-19 interventions (red) and estimated changes from the SIRS model (black). Solid lines and shaded regions represent fitted posterior median and 95% credible intervals. (C, F, I, L) True intrinsic resilience of the seasonally unforced system (vertical lines) and the posterior distribution of the inferred intrinsic resilience from the SIRS model (density plots).

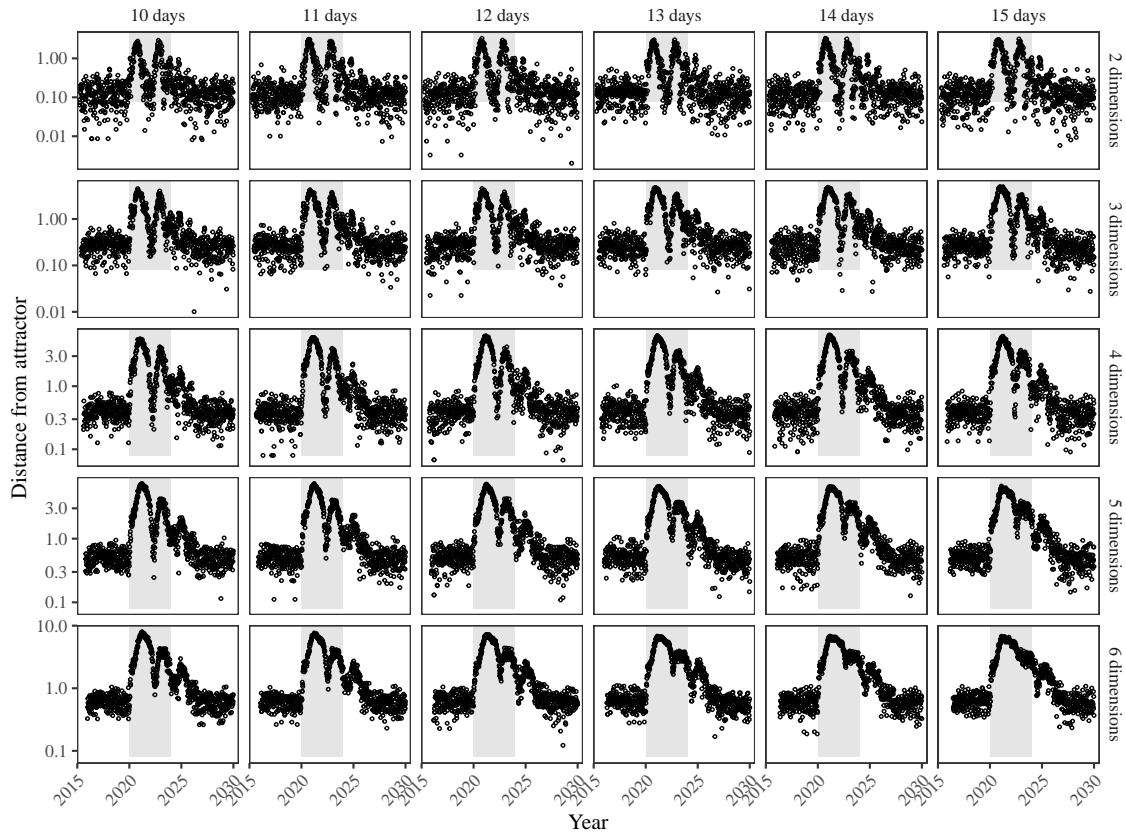


Figure S6: Sensitivity of the distance from attractor to choices about embedding lags and dimensions. Sensitivity analysis for the distance-from-attractor time series shown in Figure 3E in the main text by varying the embedding lag between 10–15 days and embedding dimensions between 2–6 dimensions.

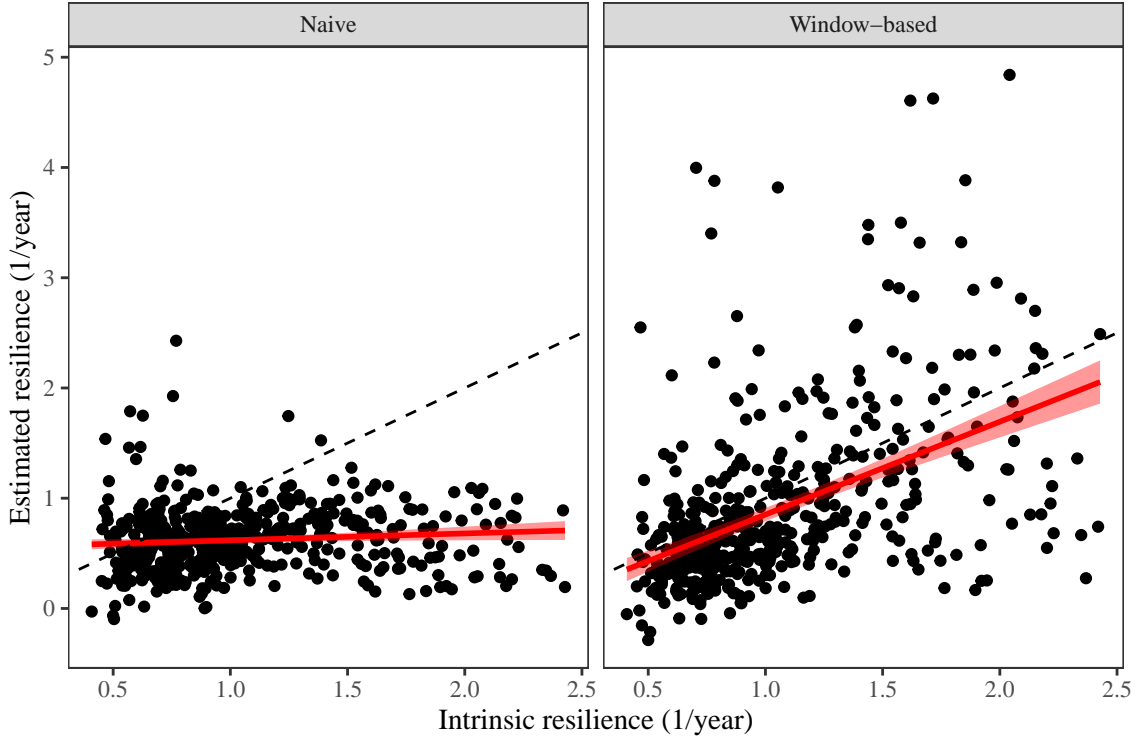


Figure S7: Impact of fitting window selection on the estimation of empirical resilience. We simulate 500 epidemics using stochastic SIRS model with randomly drawn parameters and randomly generated intervention impacts. For each simulation, we reconstruct the empirical attractor based on the approach outlined in Figure 3 and estimate the distance from attractor. The naive approach fits a linear regression on a log scale, starting from the maximum distance until the end of the time series. The window-based approach tries to select an appropriate window by smoothing the distance estimates and finding a time period when the smoothed time series crosses pre-determined threshold, relatively to the maximum distance; then, a linear regression is fitted by using the raw distance within this time period.

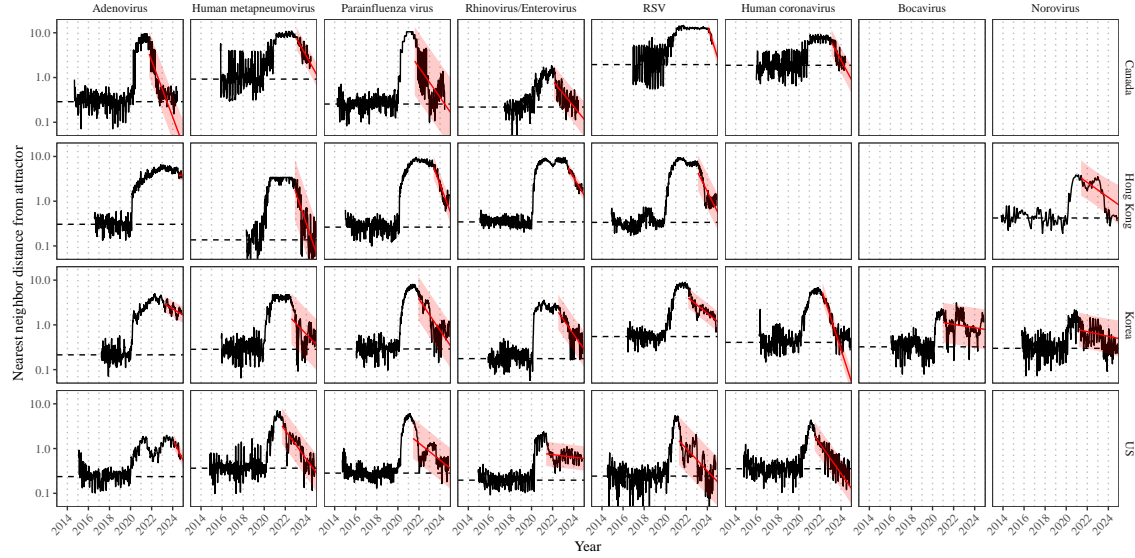


Figure S8: Estimated time series of distance from attractor for each pathogen across Canada, Hong Kong, Korea, and the US. Black lines represent the estimated distance from attractor. Red lines and shaded regions represent the linear regression fits and corresponding 95% confidence intervals. Dashed lines represent the average of the pre-pandemic nearest neighbor distances.

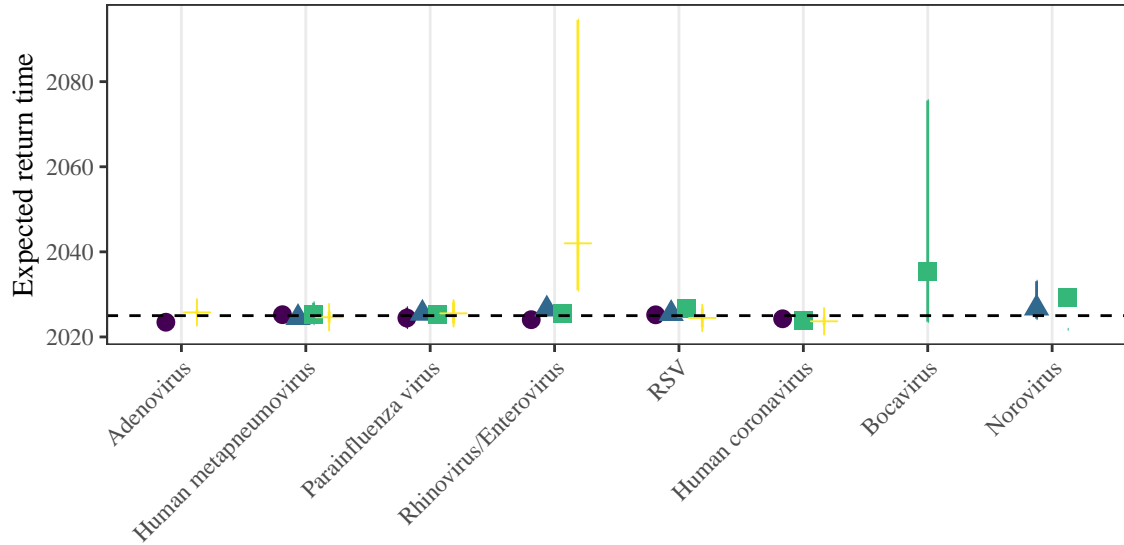


Figure S9: **Predicted timing of when each pathogen will return to their pre-pandemic cycles (zoomed out).** The dashed line in panel B indicates the end of 2024 (current observation time). Error bars represent 95% confidence intervals.

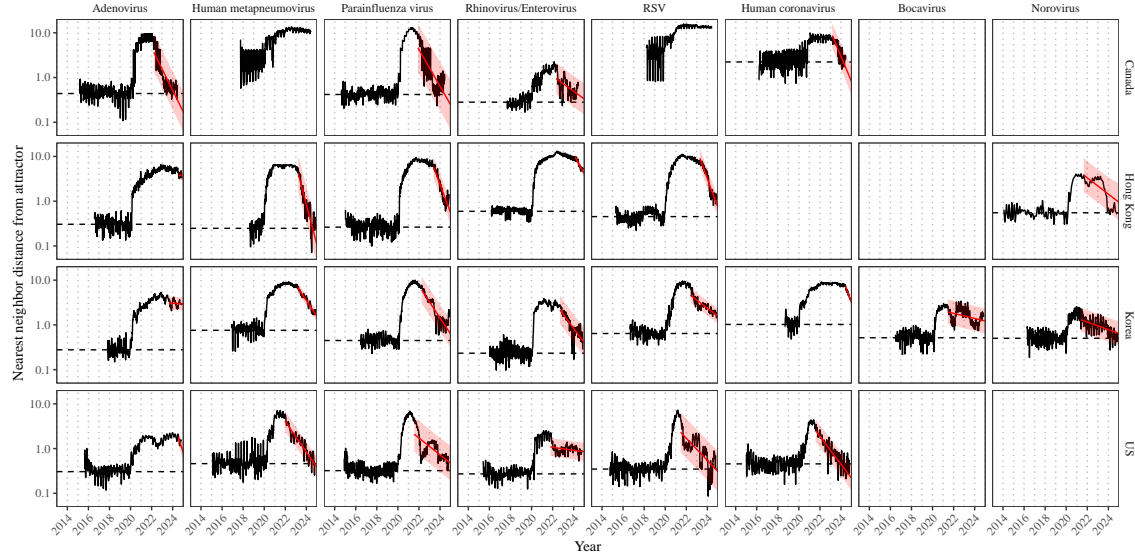


Figure S10: Estimated time series of distance from attractor for each pathogen across Canada, Hong Kong, Korea, and the US using higher embedding dimensions. Black lines represent the estimated distance from attractor. Red lines and shaded regions represent the linear regression fits and corresponding 95% confidence intervals. Dashed lines represent the average of the pre-pandemic nearest neighbor distances. A lower threshold is used for determining embedding dimensions with the false nearest neighbors approach, thereby yielding a higher embedding dimension.

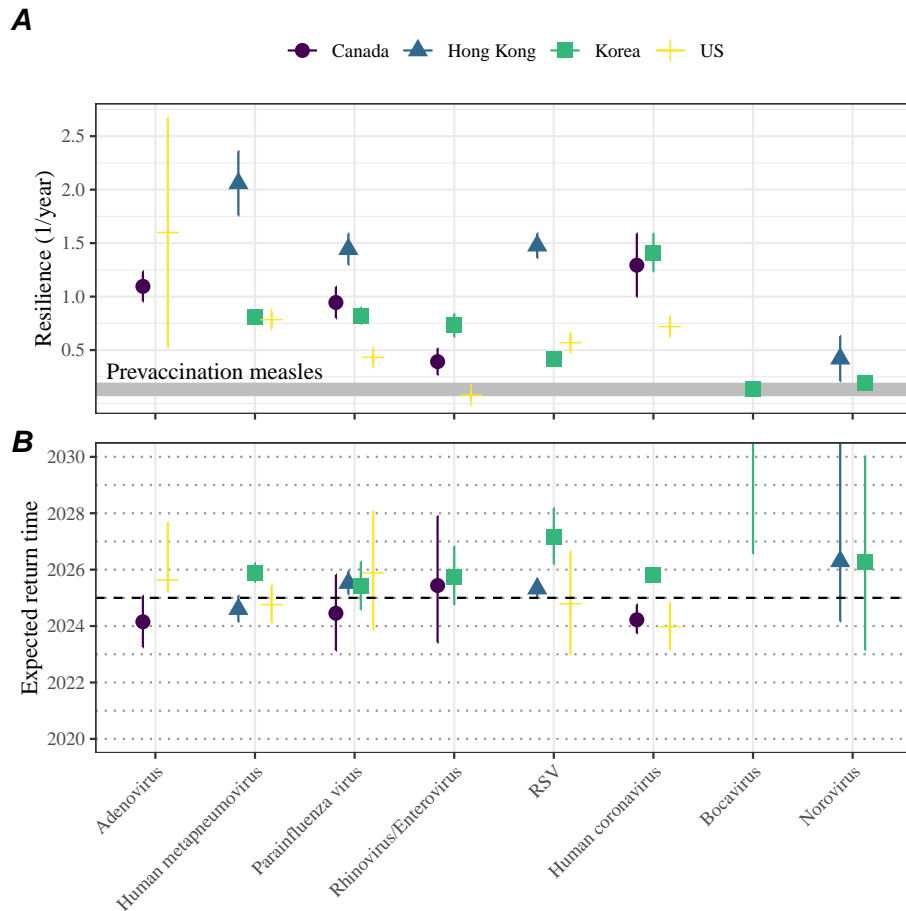


Figure S11: **Summary of resilience estimates using higher embedding dimensions.** (A) Estimated pathogen resilience. The gray horizontal line represents the intrinsic resilience of pre-vaccination measles dynamics. (B) Predicted timing of when each pathogen will return to their pre-pandemic cycles. The dashed line in panel B indicates the end of 2024 (current observation time). Error bars represent 95% confidence intervals. A lower threshold is used for determining embedding dimensions with the false nearest neighbors approach, thereby yielding a higher embedding dimension.

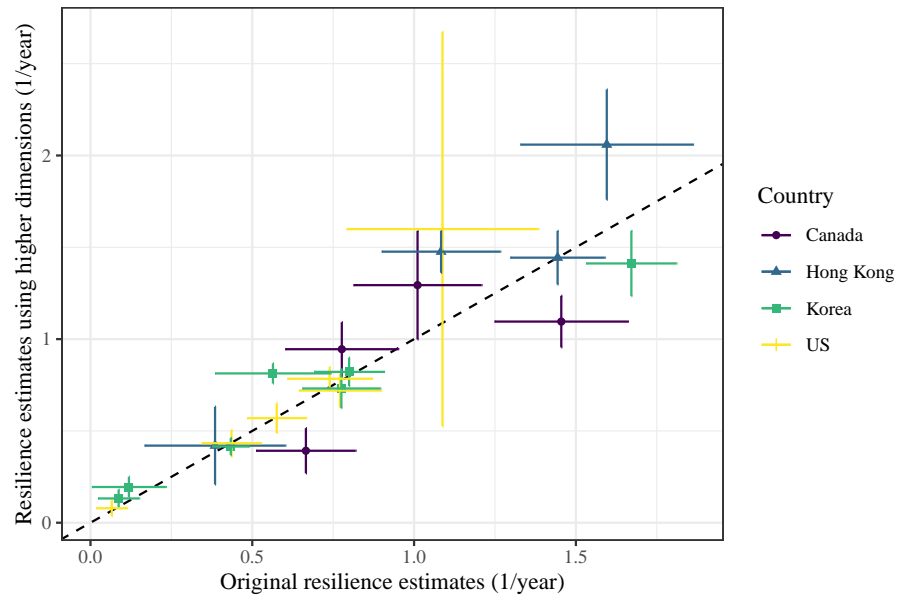


Figure S12: **Comparison of resilience estimates.** Each point represents a resilience estimate for a specific pathogen at a specific country. The x values represent the original resilience estimates presented in Figure 4. The y values represent the original resilience estimates presented in Supplementary Figure S11.

644 References

- 645 [1] Rachel E Baker, Sang Woo Park, Wenchang Yang, Gabriel A Vecchi, C Jessica E
646 Metcalf, and Bryan T Grenfell. The impact of COVID-19 nonpharmaceutical
647 interventions on the future dynamics of endemic infections. *Proceedings of the*
648 *National Academy of Sciences*, 117(48):30547–30553, 2020.
- 649 [2] Gabriela B Gomez, Cedric Mahé, and Sandra S Chaves. Uncertain effects of the
650 pandemic on respiratory viruses. *Science*, 372(6546):1043–1044, 2021.
- 651 [3] Mihaly Koltai, Fabienne Krauer, David Hodgson, Edwin van Leeuwen, Marina
652 Treskova-Schwarzbach, Mark Jit, and Stefan Flasche. Determinants of RSV
653 epidemiology following suppression through pandemic contact restrictions. *Epi-*
654 *demics*, 40:100614, 2022.
- 655 [4] Sang Woo Park, Brooklyn Noble, Emily Howerton, Bjarke F Nielsen, Sarah
656 Lentz, Lilliam Ambroggio, Samuel Dominguez, Kevin Messacar, and Bryan T
657 Grenfell. Predicting the impact of non-pharmaceutical interventions against
658 COVID-19 on *Mycoplasma pneumoniae* in the United States. *Epidemics*,
659 49:100808, 2024.
- 660 [5] Stephen M Kissler, Christine Tedijanto, Edward Goldstein, Yonatan H Grad,
661 and Marc Lipsitch. Projecting the transmission dynamics of SARS-CoV-2
662 through the postpandemic period. *Science*, 368(6493):860–868, 2020.
- 663 [6] Rachel E Baker, Chadi M Saad-Roy, Sang Woo Park, Jeremy Farrar, C Jessica E
664 Metcalf, and Bryan T Grenfell. Long-term benefits of nonpharmaceutical inter-
665 ventions for endemic infections are shaped by respiratory pathogen dynamics.
666 *Proceedings of the National Academy of Sciences*, 119(49):e2208895119, 2022.
- 667 [7] Eric J Chow, Timothy M Uyeki, and Helen Y Chu. The effects of the COVID-19
668 pandemic on community respiratory virus activity. *Nature Reviews Microbiol-*
669 *ogy*, 21(3):195–210, 2023.
- 670 [8] Edward A Bender, Ted J Case, and Michael E Gilpin. Perturbation experiments
671 in community ecology: theory and practice. *Ecology*, 65(1):1–13, 1984.
- 672 [9] Anthony R Ives and Stephen R Carpenter. Stability and diversity of ecosystems.
673 *science*, 317(5834):58–62, 2007.
- 674 [10] Marten Scheffer, Jordi Bascompte, William A Brock, Victor Brovkin, Stephen R
675 Carpenter, Vasilis Dakos, Hermann Held, Egbert H Van Nes, Max Rietkerk,
676 and George Sugihara. Early-warning signals for critical transitions. *Nature*,
677 461(7260):53–59, 2009.
- 678 [11] Stuart L Pimm. The structure of food webs. *Theoretical population biology*,
679 16(2):144–158, 1979.

- 680 [12] Michael G Neubert and Hal Caswell. Alternatives to resilience for measuring
681 the responses of ecological systems to perturbations. *Ecology*, 78(3):653–665,
682 1997.
- 683 [13] Lance H Gunderson. Ecological resilience—in theory and application. *Annual
684 review of ecology and systematics*, 31(1):425–439, 2000.
- 685 [14] Vasilis Dakos and Sonia Kéfi. Ecological resilience: what to measure and how.
686 *Environmental Research Letters*, 17(4):043003, 2022.
- 687 [15] Jeanne C Chambers, Craig R Allen, and Samuel A Cushman. Operationalizing
688 ecological resilience concepts for managing species and ecosystems at risk.
689 *Frontiers in Ecology and Evolution*, 7:241, 2019.
- 690 [16] Georgiy V Bobashev, Stephen P Ellner, Douglas W Nychka, and Bryan T
691 Grenfell. Reconstructing susceptible and recruitment dynamics from measles
692 epidemic data. *Mathematical Population Studies*, 8(1):1–29, 2000.
- 693 [17] Bärbel F Finkenstädt and Bryan T Grenfell. Time series modelling of childhood
694 diseases: a dynamical systems approach. *Journal of the Royal Statistical Society
695 Series C: Applied Statistics*, 49(2):187–205, 2000.
- 696 [18] Floris Takens. Detecting strange attractors in turbulence. In *Dynamical Sys-
697 tems and Turbulence, Warwick 1980: proceedings of a symposium held at the
698 University of Warwick 1979/80*, pages 366–381. Springer, 2006.
- 699 [19] Alan Hastings, Karen C Abbott, Kim Cuddington, Tessa Francis, Gabriel Gell-
700 ner, Ying-Cheng Lai, Andrew Morozov, Sergei Petrovskii, Katherine Scran-
701 ton, and Mary Lou Zeeman. Transient phenomena in ecology. *Science*,
702 361(6406):eaat6412, 2018.
- 703 [20] Matthew B Kennel, Reggie Brown, and Henry DI Abarbanel. Determining
704 embedding dimension for phase-space reconstruction using a geometrical con-
705 struction. *Physical review A*, 45(6):3403, 1992.
- 706 [21] Eugene Tan, Shannon Algar, Débora Corrêa, Michael Small, Thomas Stemler,
707 and David Walker. Selecting embedding delays: An overview of embedding
708 techniques and a new method using persistent homology. *Chaos: An Interdis-
709 ciplinary Journal of Nonlinear Science*, 33(3), 2023.
- 710 [22] Samit Bhattacharyya, Per H Gesteland, Kent Korgenski, Ottar N Bjørnstad,
711 and Frederick R Adler. Cross-immunity between strains explains the dynamical
712 pattern of paramyxoviruses. *Proceedings of the National Academy of Sciences*,
713 112(43):13396–13400, 2015.

- 714 [23] Bryan T Grenfell, Ottar N Bjørnstad, and Bärbel F Finkenstädt. Dynamics of
715 measles epidemics: scaling noise, determinism, and predictability with the TSIR
716 model. *Ecological monographs*, 72(2):185–202, 2002.
- 717 [24] Virginia E Pitzer, Cécile Viboud, Vladimir J Alonso, Tanya Wilcox, C Jessica
718 Metcalf, Claudia A Steiner, Amber K Haynes, and Bryan T Grenfell. Environmental
719 drivers of the spatiotemporal dynamics of respiratory syncytial virus in
720 the United States. *PLoS pathogens*, 11(1):e1004591, 2015.
- 721 [25] Katharine R Dean, Fabienne Krauer, Lars Walløe, Ole Christian Lingjærde, Bar-
722 Barbara Bramanti, Nils Chr Stenseth, and Boris V Schmid. Human ectoparasites
723 and the spread of plague in Europe during the Second Pandemic. *Proceedings
724 of the National Academy of Sciences*, 115(6):1304–1309, 2018.
- 725 [26] Margarita Pons-Salort and Nicholas C Grassly. Serotype-specific immunity
726 explains the incidence of diseases caused by human enteroviruses. *Science*,
727 361(6404):800–803, 2018.
- 728 [27] Sarah Cobey and Edward B Baskerville. Limits to causal inference with state-
729 space reconstruction for infectious disease. *PloS one*, 11(12):e0169050, 2016.
- 730 [28] Edward Goldstein, Sarah Cobey, Saki Takahashi, Joel C Miller, and Marc Lip-
731 sitch. Predicting the epidemic sizes of influenza A/H1N1, A/H3N2, and B: a
732 statistical method. *PLoS medicine*, 8(7):e1001051, 2011.
- 733 [29] Bob Carpenter, Andrew Gelman, Matthew D Hoffman, Daniel Lee, Ben
734 Goodrich, Michael Betancourt, Marcus A Brubaker, Jiqiang Guo, Peter Li,
735 and Allen Riddell. Stan: A probabilistic programming language. *Journal of
736 statistical software*, 76, 2017.
- 737 [30] Stan Development Team. RStan: the R interface to Stan, 2024. R package
738 version 2.32.6.